# Montanuniversität Leoben

# Influence of pulsed bias on CrN coatings prepared by reactive magnetron sputtering

Diploma Thesis
by
Stephan Grasser

This work has been carried out at the Department of Physical Metallurgy and Materials Testing, University of Leoben, Austria.

## Affidavit

I declare in lieu of oath, that I wrote this thesis and performed the associated research myself, using only literature cited in this volume.

Leoben, May 2, 2008

# Acknowledgment

I would like to thank Univ.-Prof. DI Dr. Helmut Clemens, Head of the Department of Physical Metallurgy and Materials Testing for giving me the opportunity to conduct this work at his department.

My sincerest gratitude is due to ao. Univ.-Prof. DI Dr. Christian Mitterer, Head of the Thin Film Group at the Department of Physical Metallurgy and Materials Testing, for the confidence he showed in admitting me to his work group.

I am very grateful to my supervisors DI Dr. Rostislav Daniel and Dr.-Ing. Claudia Walter for the interesting discussions and especially for their endless patience and kindness.

I would also like to thank DI Dr. Gert Gassner who taught me the first steps in the fragile world of thin films.

Many thanks to all my colleagues (past and present) in the Thin Film Group for their valuable discussions in all matters.

Appreciation is also extended to Ms. Hilde Stopar, who was always ready to help and support me and giving me an open ear for my problems.

My final thanks are due to my parents and friends for their love, friendship and support. Without them, everything would have been far more difficult.

# Contents

# 1 Introduction

In the realm of high technology, the surface and surface near region of a component is one of the most important engineering factors. Hence, the whole engineering world is in constant demand of high performance surface treatments in order to modify and/or improve coating properties like wear and corrosion resistance, the optical and decorative behavior, the oxidation-stability as well as providing a defined-friction behavior [1–3].

In the field of wear and corrosion resistant hard coatings, physical vapor deposition (PVD) is one of the most commonly utilized techniques in order to apply protective coatings on a solid surface. In PVD processes, the deposition of the coatings is based on the condensation of particles from the vapor phase and subsequent growth. Here, the number and the energy of the impinging particles are crucial to the development of the microstructure and thus the properties of the coating [4–6].

The chosen Cr-N system is an important and well understood deposition system offering a good wear and corrosion resistance especially at elevated temperatures [7–10]. Within this work, the attempt was made to combine the positive effects of plasma based electron bombardment (PBEB) as well as ion bombardment in order to bring forward the influence of two different kinds of particles impinging on the surface in rapid succession (in the range of kHz) on the microstructure and mechanical properties of CrN coatings. For this purpose PBEB and ion bombardment was applied in various quantities during reactive unbalanced magnetron deposition of CrN coatings on silicon. During particle bombardment, energy is introduced into the system in the shape of momentum transfer from the impinging particles to the coating. PBEB is considered to induce a more general annealing effect on the coating, resulting in the activation of energy dependent processes like surface, grain boundary and bulk diffusion as well as the chemical activation of the involved species (especially the dissociation of $N_2$). On the contrary, heavy particles (like Ar) impinging on the coating surface not only introduce energy into the coating but also penetrate the surface layers causing distortions and defects within the lattice. Thus, they increase the nucleation rate and consequently decrease the average grain size as well as inhibit the formation of columnar structures with rough surfaces.

Due to the opposed nature of the involved processes in combination with differing thresholds, reflecting the complexity of the underlaying mechanisms, a careful examination of the results will be necessary in order to determine the dominating processes and identify the overall effects on the microstructure and mechanical properties of the investigated CrN coatings.

# 2 Physical Vapor Deposition

Physical vapor deposition processes are atomistic processes in a low pressure or vacuum environment commonly used for the deposition of coatings. During deposition, material from a solid or liquid source is vaporized by evaporation or momentum transfer and transported in a form of a vapor to a substrate where it condenses and subsequently forms a coating [4–6]. PVD processes are very versatile allowing the deposition of a wide variety of coatings of various elemental compositions which makes them commonly used deposition techniques.

PVD processes can be classified according to the mechanism of vapor generation in two categories: (i) Evaporation and (ii) sputtering [5, 11]. In **evaporation** processes a heat source is utilized to vaporize the material. It is heated in different ways, typically by resistance heating, induction heating, arc discharge, or with assisting electron or pulsed laser beam. Evaporation is usually conducted at low pressures of $10^{-8}$ to $10^{-3}$ Pa. Hence, the mean free path of the vaporized atoms and molecules is very large and the particles can reach the substrate with little or no collisions with atoms and molecules of the working gases in the space between a source and a substrate. The coatings tend to have low-strength structures and are mainly used in optical, electronic and decorative applications [4, 11, 12]. **Sputtering** is a vaporization process where surface atoms are ejected from the target due to bombardment of the surface by energetic ions. Often argon ions originating from a glow discharge and subsequently accelerated by an electrical field are used to bombard the target surface. Multiple modifications are in use, usually optimizing the flux and energy of impinging particles, thus modifying the growth of the coating and subsequently the morphology of the structure in a desirable way [12, 13].

## 2.1 Fundamentals of Plasma

### 2.1.1 Definition

Langmuir coined in 1928 the term *plasma* for ionized gas [14]. Plasmas can be found in nature, in the shape of the soft glow of the Aurora Borealis or the flash of a lightning bolt, or can be technically generated by low-pressure gas discharges in fluorescent light tubes or, like in this work, in deposition chambers for surface engineering purposes. Plasmas are by far the most common phase of matter in the universe and are often referred to the fourth state of matter [5].

In order to distinguish a plasma from any gas which shows some small degree of ionization a plasma can be defined more rigorously as a gaseous medium containing charged and neutral particles, characterized by a collective behavior [15]. Electrons, ions and charged molecules are examples for charged particles whereas atoms and molecules, both in their ground or excited energy states are examples for neutral particles, respectively. Due to the motion of the charged particles, local concentrations of positive and negative electric charges are caused. These charge build-up can affect the motion of electrons and ionized particles far away from the charge concentration by Coulomb interactions giving the plasma its characteristic collective behavior [13].

### 2.1.2 Plasma Chemistry

Plasma is an energetic environment where collisions between particles may cause excitation, ionization and dissociation processes as well as penning ionization and excitation, charge exchange, photoionization and excitation, ion-electron recombination or the generation of unique species like $O_3$. Which process occurs depends amongst others on the cross-sections and the threshold energies of the individual physical or chemical process [4].

### 2.1.3 Characteristic Plasma Parameters

#### Degree of Ionization

In many cases only a fraction of the gaseous matter in a PVD processing plasma is ionized, i. e. the atoms have lost or gained electrons. Furthermore, those plasmas are usually in a quasi-neutral state meaning that the number of positive and negative charge carriers is equal: $n_i = n_e = n$, where $n$ is the charge carrier density. Thus, the degree of ionization $\alpha$ can be defined as

$$\alpha = \frac{n}{n_n + n}, \tag{2.1}$$

where $n$ and $n_n$ are density of charge carriers and neutrals, respectively. Commonly used low-pressure plasmas ($10^{-3}$ mbar) show charge carrier densities between $10^9$ to $10^{12}$ cm$^{-3}$ and the degree of ionization typically ranges from $10^{-6}$ to $10^{-3}$ [15, 16].

### Plasma Temperature

The plasma temperature represents the mean translational energy of the particles. In thermal equilibrium an ideal gas has particles with a range of different velocities whose velocity distribution can be best described by a Maxwellian distribution. The relation between the average energy $E_{av}$ and the plasma temperature $T_p$ can be given by

$$E_{av} = \frac{3}{2} k_B T_p, \tag{2.2}$$

where $k_B$ corresponds to the Boltzmann's constant [15]. Low-pressure plasmas are usually far from thermal equilibrium and each species can have a different temperature at the same time which corresponds to different kinetic energy of the particles. An applied power mainly influences the electrons due to their lighter mass and the electron energy is typically in the range of 1 to 10 eV [13]. According to $k_B \cdot T_p = 1\,\text{eV} = 1.6022 \times 10^{-19}\,\text{J}$ the electron temperature corresponding to an electron energy of 1 eV is 11 605 K [17]. Nevertheless, the amount of heat transferred by the electrons to the gas is low because of the very low heat capacity and very low density of electrons in the plasma. Therefore these plasmas are also considered cold plasmas [16].

### Debye Length

The charged particles in the plasma react to local changes in the electrical field in the plasma screening off the Coulomb field within a certain distance. This response is called Debye shielding or self shielding and the characteristic length scale is termed Debye length. Electrons react much faster than ions to disturbances in the electrical field due to their lighter mass. Therefore, electrons are the determining species for the Debye length $\lambda_D$ which can be given by

$$\lambda_D = \sqrt{\frac{\epsilon_0 k_B T_e}{n_e e^2}}, \tag{2.3}$$

where $\epsilon_0$ is the permittivity of free space, $k_B \cdot T_e$ is a term describing the electron energy, $n_e$ and $e$ are the electron density and charge, respectively. The response to perturbations of the electric field in the plasma will be through oscillations of the electrons. The frequency of these electron oscillations is called plasma frequency $\omega_p$ and can be calculated as:

$$\omega_p = \sqrt{\frac{n_e e^2}{m_e \epsilon_0}}. \tag{2.4}$$

Here, $m_e$ is the electron mass. Disturbances of the plasma with frequencies lower than the plasma frequency will be shielded out. A typical low-pressure plasma with an electron density of $10^{10}$ cm$^{-3}$ has a plasma frequency of $9 \times 10^8$ Hz [15, 16].

#### Plasma Sheath

When charged particles hit the grounded confinement, they recombine and are lost for the plasma system. Electrons usually have a higher thermal velocity than ions, thus they are lost faster and leave the plasma with a net positive charge in the vicinity of the surface. Due to Debye shielding an electric field develops near the surface in such way as to make the net current zero. Within this potential variation (the so called *sheath*) the electron density is very low compared to the bulk of the plasma. Consequently, only low levels of excitations of the gas species occur, and hence the area appears dark. The plasma is therefore always at a positive potential (*plasma potential* $V_p$) relative to any grounded surface in contact with it. If the surface is electrically floating and the plasma is in contact with a large-area grounded surface, the floating surface will be negative with respect to the ground (*floating potential* $V_f$). Low-voltage sheaths have typical dimensions of a few Debye lengths [4, 13, 15, 16].

### 2.1.4 Plasma Generation

In order to ignite a stable discharge process an external power source, e. g. electrical or thermal, is necessary. Figure 2.1 shows a common direct current (DC) diode setup. Here, a DC voltage is applied between two conductive electrodes and a power supply is used to sustain the electric field [15]. Such, free electrons which are always present due to natural background radiation or cosmic rays are accelerated to high energies. The fast electrons (primary) are capable of ionizing atoms of the background gas (usually a noble gas like Ar) by electron-atom collisions releasing more electrons [4, 13]. Furthermore, the electrons and ionized atoms are accelerated towards the electrodes where secondary electrons are emitted due to the ion or electron bombardment [4]. In order

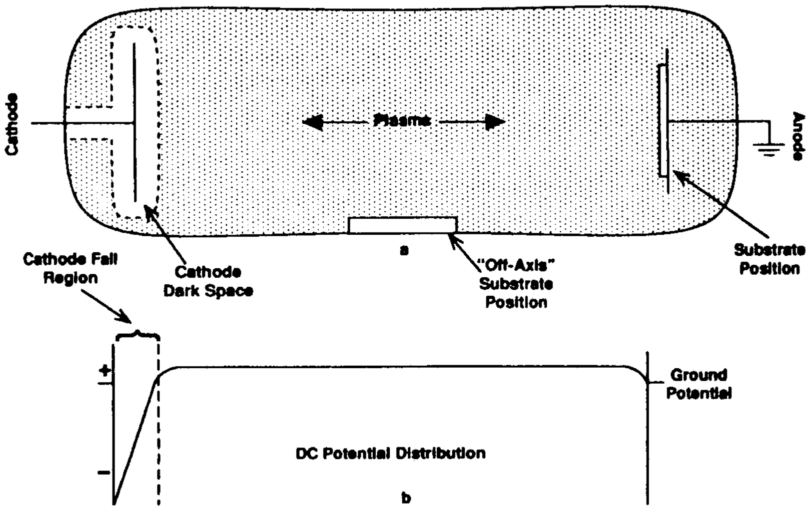

Fig. 2.1: Scheme and characteristic potential distribution in a DC glow-discharge [4].

to maintain a stable discharge process, enough charged particles must be generated to balance reduction of the plasma density due to recombination, radiation and other loss mechanisms.

## 2.2 Sputtering

*"Sputtering involves the physical vaporization of atoms from a surface by momentum transfer from bombarding energetic atomic-sized particles"* [4]. Positive ions, typically $Ar^+$ from the near edge of the plasma region are attracted from the cathode potential. The positive ions are accelerated across the cathode fall region and impinge on the cathode – also called target. Due to momentum transfer atoms from the target are knocked out of the surface. The atoms are electrically neutral and not affected by the electric field. After collisions with plasma particles, the target atoms usually recondense at the substrate as well as the chamber walls. The average number of atoms ejected from the target per incident ion is called sputtering yield. The sputtering yield rises with an increasing number of the impinging atoms. However, a high ionization yield decreases the mean free path of the sputtered atoms propagating the number of collisions which reduces the sputtering yield [4, 5]. Figure 2.2 shows an overview about the events which occur on a surface being bombarded with energetic atom-sized particles.

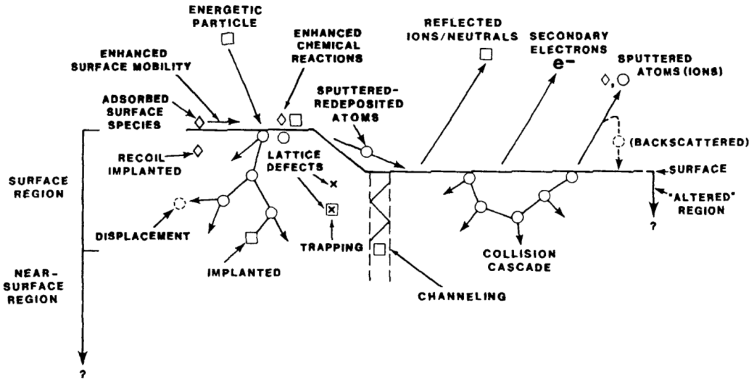

Fig. 2.2: Physical and chemical reactions to be found at a solid surface exposed to particle bombardment [4].

## 2.2.1 Diode Sputtering

The simplest sputtering system is the DC diode setup [5, 11, 13]. Here, the sputtering target is the cathode, which is usually water-cooled, and the substrate is placed on the anode, both usually facing each other, as can be seen in Fig. 2.3. A potential is applied at the target and the anode is often grounded. The target performs usually two functions during deposition, one as the source of the coating material and the other as source of secondary electrons. The secondary electrons from the target are accelerated away from the cathode. These high energy electrons are necessary to sustain the DC glow discharge by colliding with atoms, and consequently producing ions. DC diode discharges are

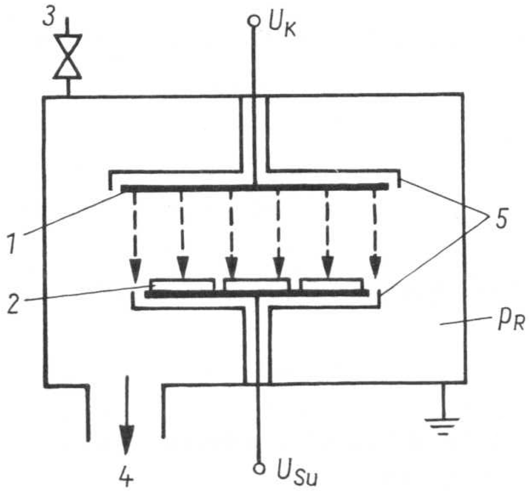

Fig. 2.3: DC diode sputtering array. $U_K$... Cathode potential, $p_R$... Pressure, $U_{Su}$... Bias potential, 1... Target, 2... Substrates, 3... Gas inlet, 4... Evacuation system, 5... Shield [18].

usually operated with argon plasmas at a pressure between approximately 1 and 10 Pa. A minimum gas pressure is necessary to establish a glow discharge. On the other hand, if the pressure is too high, material sputtered from the surface will be scattered back to the electrode and a coating grows with very low deposition rates if any. The DC diode setup allows the generation of a very uniform plasma over a large area. Though, the deposition rate is very low and the substrates becomes very hot due to particle bombardment, as the plasma is very close to both cathode and anode [4, 5, 11, 13, 18, 19].

### 2.2.2 Unbalanced Magnetron Sputtering

In order to overcome the disadvantages of the DC diode setup a magnetron device can be utilized. Here, magnetic $\vec{B}$ and electric $\vec{E}$ fields are employed both to restrict and intensify the plasma to the area near the target. Thereby, increasing the ionization efficiency near the target, a stable discharge can be maintained at lower gas pressures. Thus, the mean free path of the sputtered atoms increases and the collisions and scattering of the sputtered atoms in the gas phase are lessened. Consequentially, for the same electrode spacing and minimum target voltage, a higher deposition rate can be obtained.

Several magnetron configurations are available, whereas the planar magnetron configuration with parallel target and anode electrode surfaces is the most common [5]. Figure 2.4 shows a schematic of a magnetron in circular planar configuration. In this geometry, small permanent magnets are arranged in the back of the target. In doing so, a *looping* magnetic field $\vec{B}$ is generated which, in combination with an electric field $\vec{E}$ transmitted through the cathode, forces charged particles due to the $\vec{E} \times \vec{B}$ drift to

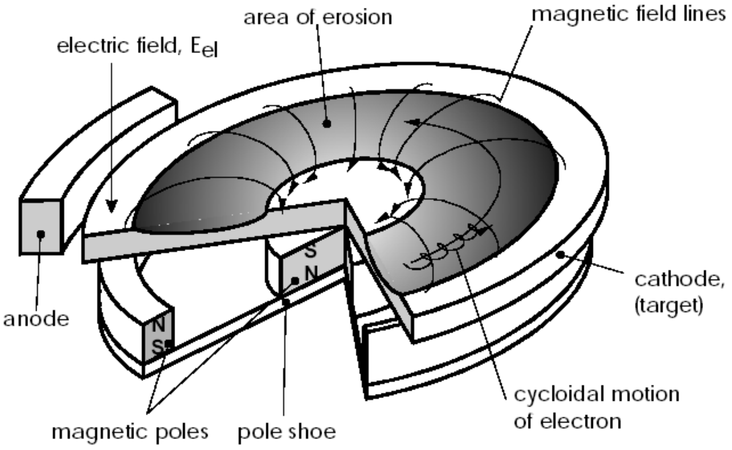

Fig. 2.4: Magnetron in circular planar configuration with racetrack area of erosion [20].

follow helical paths around the magnetic field lines. The orbit radius of ions is much bigger than that of electrons which is usually quite small with respect to the dimensions of the system. Hence, only electrons are considered. The electrons are confined near the electrode and form a drifting, circulating current, often called *racetrack*. The retention time of the electrons near the target is increased and the loss of electrons due to wall reactions is minimized. The sputter erosion is restricted to the racetrack area.

Depending on the course of the magnetic field lines between the inner and outer magnets two arrangements can be distinguished (Fig. 2.5): (i) Conventional balanced configuration (CBM) and (ii) unbalanced configuration (UBM). If all magnetic field lines loop, the magnetron configuration is called balanced and most of the electrons and therefore the plasma are confined near the target surface. In the later case, the magnetic field lines are partially open to the substrate. Electrons then create a plasma away from the target surface. Such, ions for surface bombardment of the substrates are generated as well as reactive gas is activated for the reactive deposition process [4, 5, 13, 15, 18, 21]. In order to influence the level of the magnetic unbalance/balance and accordingly vary the level of ion bombardment of the growing coating, variable magnetrons or external Helmholtz coils can be utilized [22–26].

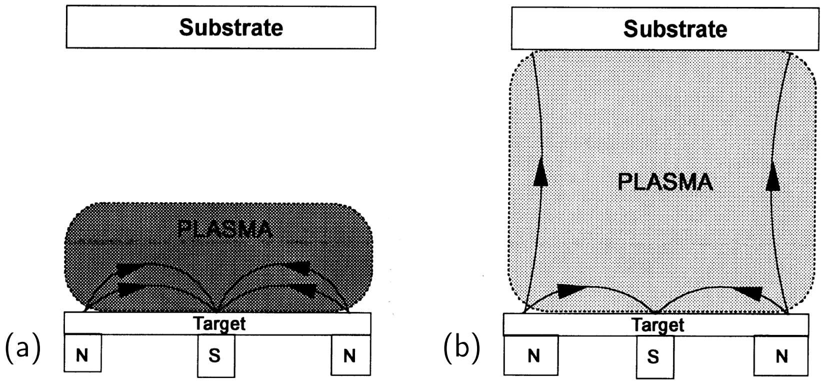

Fig. 2.5: Magnetron in balanced (a) and unbalanced (b) configuration [23].

### 2.2.3 Reactive Magnetron Sputtering

Magnetron sputtering is a powerful and flexible technique which can be used to coat virtually any workpiece with a wide range of materials – any solid metal or alloy and a variety of compounds. Single elements can be easily deposited by sputtering single element targets. Alloys can be fabricated using several single elemental targets (also called co-sputtering), segmented targets where the segments consist of each of the components of the alloy or alloyed targets. Though each alloy component in an alloyed target sputters with a different yield, the differences are negligible and the stoichiometry of the coating mainly reflects the composition of the targets used for deposition [5, 13].

Coatings made of compounds like oxides, nitrides, carbides or sulfides are usually sputter deposited by reactively sputtering an elemental target in the presence of a reactive gas mixed with an inert working gas. For hard coatings like TiN or CrN usually nitrogen in its molecular state ($N_2$) is used as reactive gas. Because nitrogen is not effective in sputtering due to its low atomic mass, heavier argon gas is used to aid in sputtering. The reactions to form the compound may occur in either the gas phase or on a solid surface. Reactions in the gas phase are seldom because they usually involve 3-body-collisions which are unlikely at low pressures used for PVD processes. Reactions on solid surfaces include the formation of the compound not only on the substrates as desired but also on the chamber walls as well as on the target. The latter is also termed *target poisoning* and greatly reduces the sputtering rate and sputtering efficiency. The compound layer on the target typically possesses a lower sputtering as well as higher secondary electron emission yield compared to the pure target. The latter means that more energy of incoming ions is consumed to produce and accelerate electrons. The negative effect of target poisoning can be lessened by introducing an inert atmosphere close to the target, whereas the reactive gas inlet is placed near the substrates. Additionally, the plasma can be expanded and intensified close to the substrate in order to increase the reactivity of the substrate area as in the case of an unbalanced magnetron configuration as described above [4, 11, 13, 15].

## 2.3 Nucleation and Growth

After evaporation and traversing the space, the sputtered atoms may collide with the solid surface of the deposition chamber or the substrates. On solid surfaces impinging atoms can either simply bounce or condense on the surface (Fig. 2.6). Condensation usually requires an equal chemical nature of both impinging atom and solid surface. In most PVD processes the vapor and the solid surface are different substances. Hence, the vapor atoms will not immediately react with the surface but become loosely bonded atoms, so termed *adatoms*. These adatoms have some degree of mobility through diffusion. The mobility of the adatoms depends on their energy, the adatom-surface interactions as well as the temperature of the surface. Such, the adatoms may diffuse at the surface until they are desorbed, by sputtering or re-evaporation, or, more commonly, become trapped at low-energy lattice sites. Low-energy sites can be found at morphological

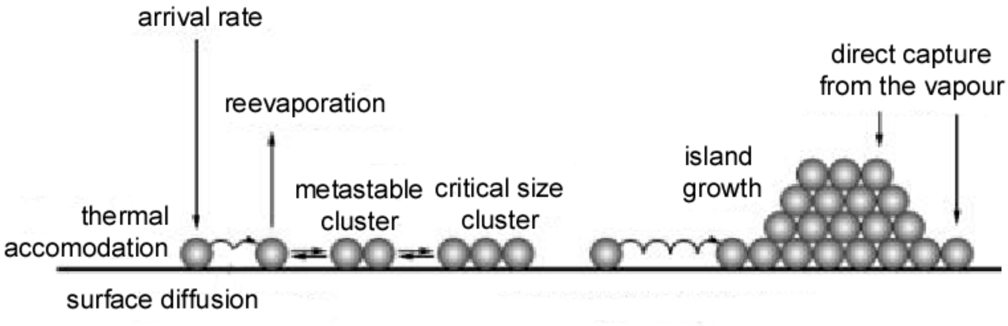

Fig. 2.6: Schematic of nucleation and growth processes at a solid surface exposed to vapor [20].

surface discontinuities such as steps or scratches and lattice defects in the surface such as point defects or grain boundaries as well as next to other surface adatoms or at surface areas which have a different chemistry or crystallographic orientation. The ratio between impinging and the finally trapped atoms is called the sticking or condensation coefficient.

When several adatoms agglomerate they may form stable clusters. These clusters are termed *nuclei* and the process *nucleation*. The number of nuclei per unit area is called nucleation density. The further enlargement of the nuclei happens either by collecting atoms which impinge on the nuclei directly or migrate over the surface to the nuclei and is termed *growth*. The growth depends on the affinity of the coating material to the substrate, the activation energy of diffusion and the binding energies between coating-coating and coating-substrate. In thermodynamic equilibrium three basic growth modes can be distinguished: Island growth (or Volmer–Weber mode), layer growth (or Frank–Van der Merve mode) and a mixed layer–island growth (or Stranski–Krastanov mode) [4, 5, 27–29].

### 2.3.1 Structure Zone Models

The microstructure is one of the most important variables influencing the properties of the coating. Due to the non-equilibrium nature of PVD processes, coatings with unique microstructure can be obtained. Hence, knowledge about the relation between deposition parameters and coating structure is essential [5, 11].

Movchan and Demchishin where the first to propose a *structure zone model* (SZM) in order to predict the morphology and microstructure of the coating, independently of the involved materials. Based on observations on very thick evaporated coatings (0.3 mm to 2 mm), the morphological structure could be related to the homologous temperature ($T_s/T_m$) of the coating [30]. Here, $T_s$ is the actual coating temperature during deposition, and $T_m$ is its melting temperature.

In 1977, THORNTON adapted this structure zone model for sputtered metal deposits by introducing, additionally to the homologous temperature, another variable, the inert sputtering gas pressure [31, 32]. Here, the pressure affects the evolution of the coating via several indirect mechanisms. An increase in gas pressure decreases the mean free path for collisions between sputtered atoms and working gas and hence the deposition flux is reduced due to gas scattering. On the other hand, a low gas pressure may densify the microstructure of the coating because of an increased energetic-particle bombardment [5]. The resulting SZM features 4 zones (1, 2, 3, T) as can be seen in Fig. 2.7.

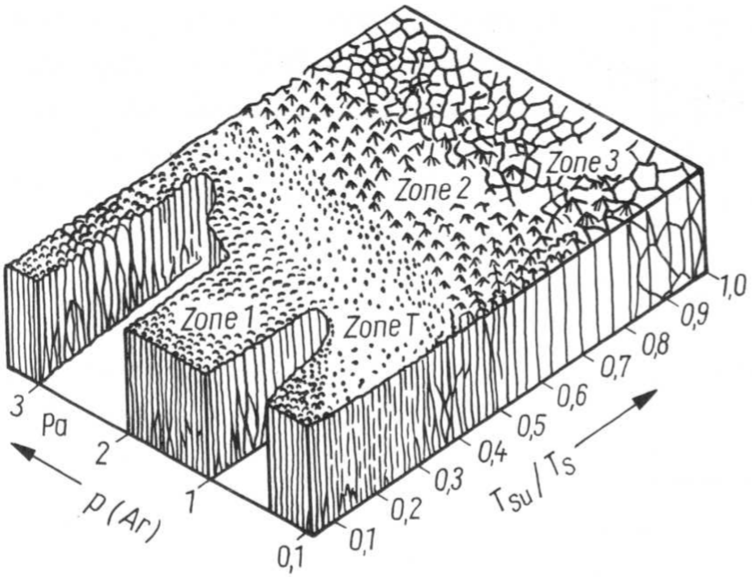

Fig. 2.7: Structure zone model proposed by THORNTON [32].

The microstructure in **Zone 1** ($T_s/T_m < 0.3$) is characterized by tapered columns and significant voids between columns. This is caused by the negligible diffusion of the trapped atoms leading to shadowing effects. Thereby, most of the sputtered flux is deposited on high points of the coating, with little material reaching the valleys. **Zone T** is considered to be a transition zone between Zone 1 and Zone 2. A small grained structure reflecting the nucleation density due to yet immobile grain boundaries is formed. When the film becomes continuous, crystallographic planes with low energy surfaces overgrow adjacent crystals having higher surface energies because of the beginning surface diffusion. A cone shaped columnar structure is typical for this competitive growth. The activation of grain boundary migration marks the beginning of **Zone 2**. Usually, it is found at a homologous temperature of $0.3 < {}^{T_s}/_{T_m} < 0.5$. The initially formed small grained structure is dissolved step by step during coalescence and in the later growth stage. Hence, the structure consists of uniform columnar grains defined by grain boundaries perpendicular to the substrate surface. The surface of Zone 2 coatings tend to have highly faceted top surfaces giving rise to a smooth but mat surface. **Zone 3** appears at a homologous temperature higher than 0.5 in pure metals. Here, additional bulk diffusion allows recrystallization, grain growth and further densification. [31–34].

In order to point out the influence of some basic growth conditions, four growth structures have been compiled assuming extreme cases of surface diffusion, condensation coefficients and nucleation (Fig. 2.8) [35]. The case of zero surface diffusion and a unity condensation coefficient is shown in Fig. 2.8 a. The initial nuclei are spherical since there is no crystal surface discrimination. A flux mostly normal to the surface will lead to the formation of a dense columnar coating structure. Commonly, this structure can be found in Zone T. In contrast, zero surface diffusion in combination with a crystallographic surface dependent condensation coefficient will result in preferred growth of particular nuclei (Fig. 2.8 b). Due to the perpendicular coating flux, isolated crystals with sharply featured surfaces are formed. A rough and open structure corresponding to Zone 1 is obtained. Infinite surface diffusion as for example in the case of elevated substrate temperatures $T_s$ redistributes the coating flux and removes any dependence on the condensation coefficient. All crystals grow with the same rate and a dense columnar Zone 2 structure with a smooth but faceted surface is formed (Fig. 2.8 c). In the case of infinite surface diffusion and periodic nucleation a structure as shown in Fig. 2.8 d may

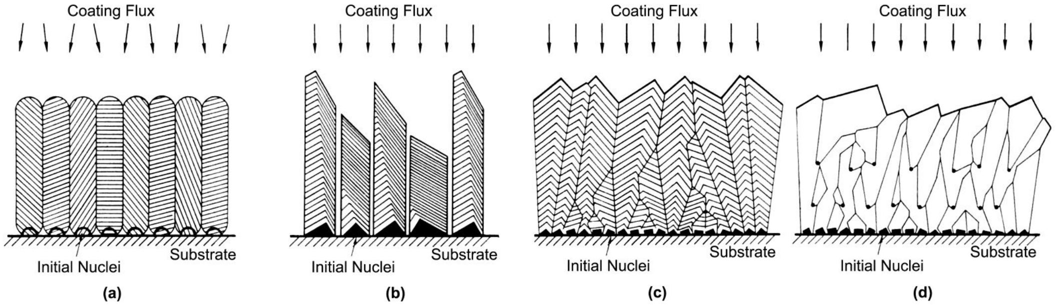

Fig. 2.8: Growth structures constructed for several extreme cases: Zero surface diffusion with unity (a) and crystallographic surface depended condensation coefficient (b), infinite surface diffusion without (c) and with periodic nucleation (d) [35].

develop. Periodic nucleation may be caused by e. g. an increased number of impinging particles especially in combination with high energy particle bombardment as well as impurities. The influence of the latter is also illustrated in Fig. 2.9. In this context not only contamination by foreign species like vapor, oxygen, and hydrocarbons but also deliberately deposited alloying elements can be considered as impurities. Figure 2.9 a shows the typical microstructure of a pure coating with respect only to the homologous temperature (ideal structure zone model) as already described above. With increasing impurity content (Fig. 2.8 b – d) a change of the zone transition temperatures as well as a grain refinement can be observed. Even very low concentrations may be already active [34, 36, 37].

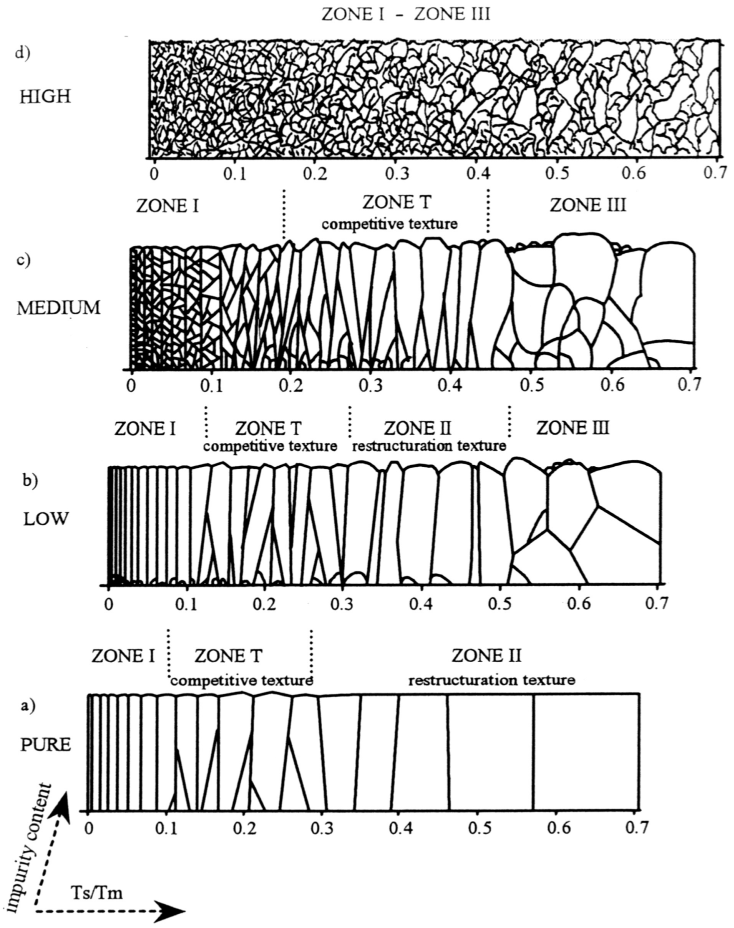

Fig. 2.9: Evolution of microstructure depending on varying content of impurities during deposition process [34].

### 2.3.2 Energetic Particle Bombardment

#### Ion bombardment

Migration and diffusion processes of the coating can be activated by energetic inputs delivered to the growing coating. Energy delivered to the coating by particle bombardment (also called atomic scale heating) and physical heating by e. g. ohmic heating of the substrates have different effects on the coating. Though particle bombardment leads to substrate heating, highly non-equilibrium processes are stimulated too. The latter may initiate a variety of reactions such as substrate surface chemistry changes, sputtering of deposited material or gas incorporations into the growing coating as well as modification of the coating morphology, crystal orientation, grain size, etc. and may result in the formation of stable and unstable materials [4, 13, 25].

The intensity of the particle bombardment is related to the residual pressure, however a direct control is limited. A minimum pressure must be maintained in order to keep the plasma burning as well as achieve a reasonable sputter yield whereas an upper limit of the pressure is given due to the increasing plasma impedance and amplified scattering events in the plasma. Hence, particle bombardment during deposition is typically conducted and controlled by the application of a bias voltage at the substrates, whereas the pressure is kept constant.

Particles utilized for this kind of surface treatment typically are: (i) Ions from the plasma or a special ion source accelerated towards the surface by an applied or self-bias or (ii) high energy neutrals which are reflected during sputtering in low-pressure deposition [4]. Assuming no external ion source is used and the mean free path is shorter than the distance between target and the substrates, then the particle bombardment consists mainly of inert gas ions (typically $\mathrm{Ar}^+$). The energy of the ions $E_i$ bombarding the surface of the growing coating corresponds approximately to the applied bias voltage $V_b$ via $E_i = e(V_b - V_p)$. Here, $V_p$ is the plasma potential which is close to that of the grounded anode and $e$ is the electronic charge. A low energy bombardment with energies in the range from several eV to about 1000 eV is called magnetron sputter ion plating, whereas surface treatment with very high energies ($E_i \gg$ keV) is called ion implantation [25, 38].

In magnetron sputter ion plating, most of the ion energy is transformed into heat in the near-surface region which increases the adatom mobility in general. A more direct influence is caused by *atomic peening* where surface atoms are struck and recoil into voids and interstitial sites in the lattice. This leads not only to a densification of the coating structure but can introduce high compressive stresses too. Furthermore, the more densely packed crystallographic planes evolute parallel to the impinging flux. At higher ion energies gaseous ions may be incorporated [4].

Considering the enhanced mobility of the adatoms due to particle bombardment, a revised and modified structure zone models has been proposed by MESSIER *et al.*. Here, the preferred Zone T is widened relative to Zone 1 and can be gained at lower deposition temperatures, Fig. 2.10 [5, 11, 13, 39, 40].

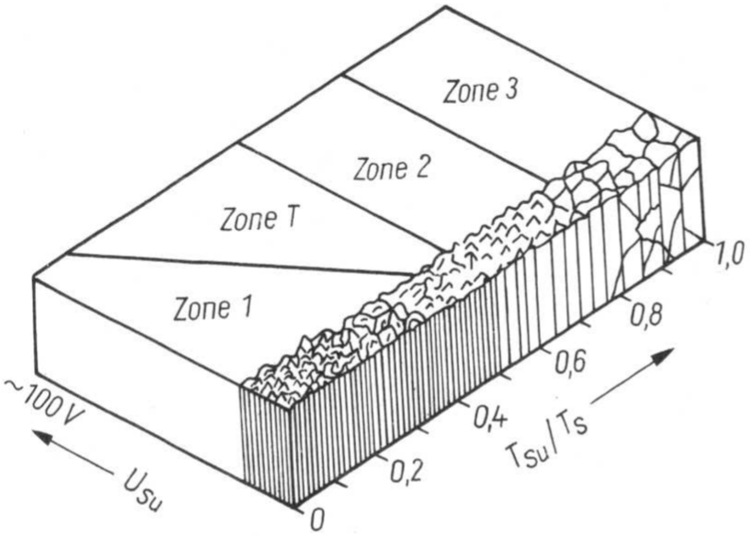

Fig. 2.10: Structure zone model modified by MESSIER *et al.* showing the effect of both bombardment and thermal-induced mobility [39].

### Electron bombardment

In contrast to a negative bias voltage, a positive voltage would result in a reduction of ion energy and finally repel incoming positive ions. Rather, electrons will be attracted which may lead to an increase in substrate surface temperature without serious sputtering effects. Hence, plasma based electron bombardment (PBEB) can be used in order to reduce the deposition temperature [41–44] as well as to conduct in-situ heat treatments [45, 46]. In the latter case, usually high voltages (kV, MV) are applied.

Based on a simple negative DC bias voltage commonly applied in PVD processes (Fig. 2.11 a), a rectangular wave voltage typically used for pulsed bias is determined by its base and reverse voltages, its period (equal to frequency$^{-1}$) and either pulse duration or duty cycle $D$ as shown in Fig. 2.11 b. The latter is given by

$$D = \frac{\tau}{T}, \tag{2.5}$$

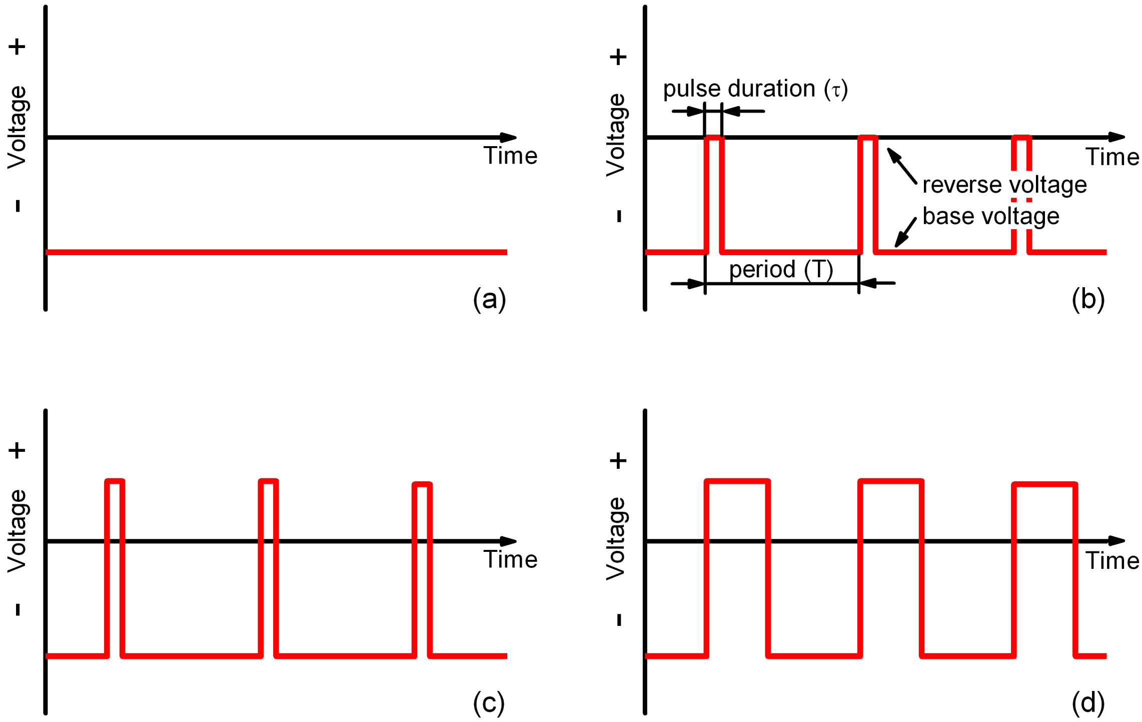

Fig. 2.11: Scheme of a DC (a), unipolar (b) and asymmetric bipolar rectangular wave voltage with short (c) and long (d) duty cycle.

where $\tau$ is the pulse duration and $T$ is the period of the rectangular waveform. If the reverse voltage is zero or negative the wave signal is called unipolar (Fig. 2.11 b). An alternating polarity of base and reverse voltage but different amplitudes, is called asymmetric bipolar (Fig. 2.11 c, d).

# 3 Chromium Nitride

## 3.1 Chromium - Cr

The ancient Greek word "χρωμα" (color, because of the many colorful compounds known for chromium) is the root for the word chromium which refers to the element with the atomic number 24. It is a d-block element forming a body-centered cubic structure ($Im\bar{3}m$) with a cell parameter of 2.91 nm as can be seen in Fig. 3.2 c. At standard conditions, chromium is a solid having a density of 7.140 $^{g}/_{mm^3}$ which is odorless, tasteless and of greyish color. Pure bulk chromium is a malleable metal with a Young's modulus of 279 GPa and a Vickers hardness of approximately 1060 MPa. It is typically obtained commercially by heating chromite ($FeCr_2O_4$) in the presence of aluminum or silicon.

## 3.2 Nitrogen - N

Nitrogen (Latin nitrogenium, where nitrum means "native soda", and genes means "forming") is used in its gaseous form where it is odorless, tasteless and colorless. It is the main fraction of air (78 Vol.-%) and plays an essential role in all biological processes. It is a p-block element which forms a diatomic gas at standard conditions. The high electronegativity of 3.04 leads to strong bonds and allows the formation of stable nitrides with transition metals [47]. Usually, nitrogen gas is acquired by the fractional distillation of liquid air, also called cryogenic air separation.

## 3.3 Chromium Nitrides

Chromium nitrides belong to the group-VI transition metal nitrides. Chromium and nitrogen can form two stable compounds – $Cr_2N$ and CrN as can be seen in Fig. 3.1. In thermal equilibrium, the hexagonal $Cr_2N$-phase (Fig. 3.2 b) is stable over a wide range of N content where the homogeneity range for the CrN-phase is very narrow, it extends from 49.5 to 50.0 at.-% N. Furthermore, CrN shows an orthogonal structure (Pnmm) for

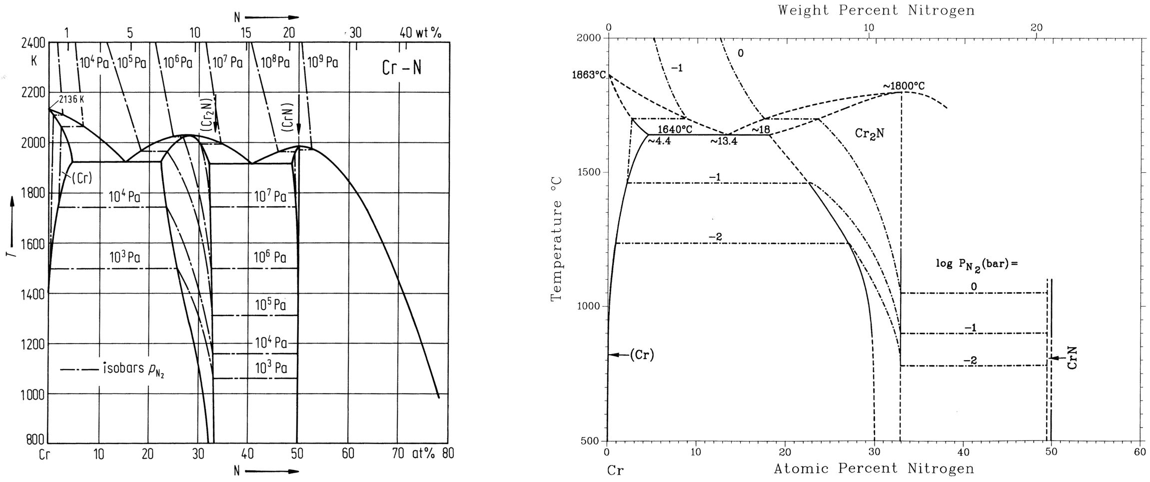

Fig. 3.1: Equilibrium phases of chromium and nitrogen [48, 49].

temperatures below 285 K and forms a cubic structure (Fm$\bar{3}$m) at higher temperatures (Fig. 3.2 a).

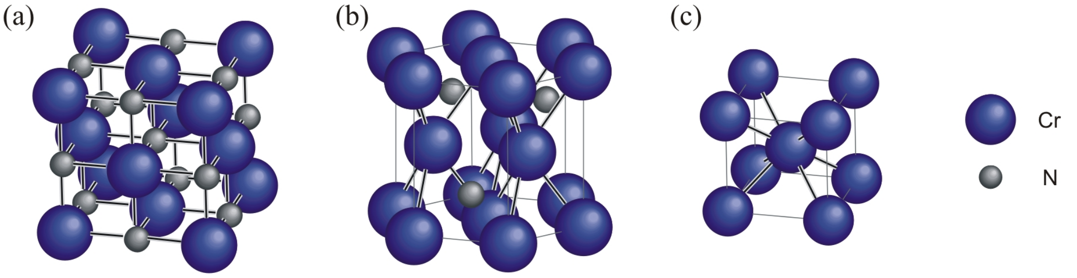

Fig. 3.2: Lattice structure of CrN – fcc (a), $Cr_2N$ – hexagonal (b), and pure Cr – bcc (c).

For non-equilibrium processes like PVD, the chemical composition of a coating depends very much on the deposition parameters. The most pronounced influence is given by the nitrogen partial pressure ($p_{N_2}/p_T$). Here, several regimes of the chemical composition of the coating can be distinguished, where the coatings are built up by single or mixed Cr, $Cr_2N$ or CrN phases. For example, Hones [50] *et al.* reported the occurrence of Cr and $Cr_2N$ at very low nitrogen partial pressures ($< 0.07$), followed by a narrow $p_{N_2}/p_T$ range existing for the deposition of $Cr_2N$ single phase. A nitrogen partial pressure higher than 0.1 leads to the formation of a two phase regime consisting of $Cr_2N$ and CrN. For $p_{N_2}/p_T$ higher than 0.15 the formation of CrN single phase is favored. However, no strict limits for the occurrence of phases can be given as the formation of the coating is influenced by many more deposition parameters, like substrate temperature, ion energy and ion-to-atom flux ratio [20, 51–54].

# 4 Experimental

## 4.1 Coating Deposition

### 4.1.1 Deposition System

All coatings for this work were deposited with a DC reactive unbalanced magnetron sputtering device at the Montanuniversität Leoben, as schematically shown in Fig. 4.1. The sputtering array was based on a Leybold Univex 300 and consisted of a steel chamber which housed a planar circular magnetron in unbalanced configuration (Gencoa PP150). A parallel target-substrate holder assembly at a target-to-substrate distance of 75 mm was used, where the target is screwed onto the water-cooled magnetron. The

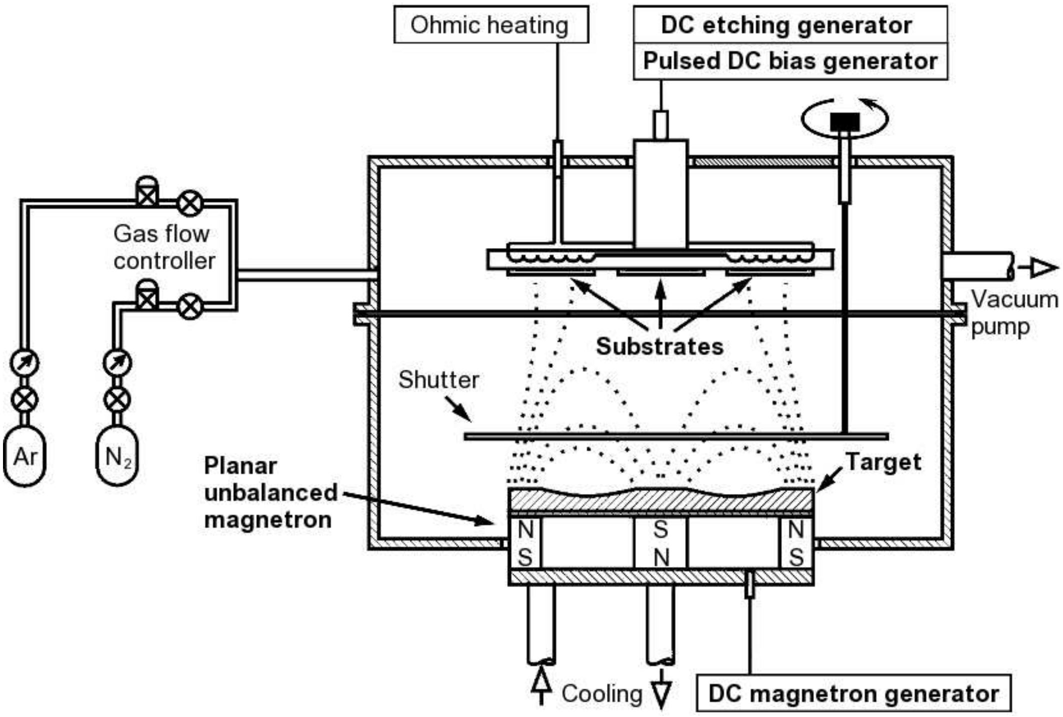

Fig. 4.1: Schematic of the reactive unbalanced magnetron sputtering device used in this work.

plasma was established by a DC ENI DCG-75E generator. The substrate was ohmicly heated. The chamber was evacuated by a two-step rotary vane vacuum pump (Balzers DUO 016B) and a turbo molecular pump (Leybold Turbovac TW 250). Substrate etching was performed by an independent DC Hippotronics 803-330 generator providing highest performance of the substrate etching process.

The substrate bias voltage serving for an enhanced growth process of the coating was supplied by an ENI RPG-50 pulsed DC plasma generator. Both DC and asymmetric bipolar pulsed modes were used for the experiments. The plasma generator was originally designed to generate the plasma with a maximum power output of 5 kW resulting from a maximum current of 10.5 A or maximum voltage of 1800 V, respectively. In the case of biasing the substrates lower energies (< 30 W) are required. Hence, the plasma generator is driven far below the designed application range. Therefore, in DC mode the voltage output shows an oscillation about the preset voltage, e. g. when set at -70 V the voltage measured at the substrate holder varied between -45 V, which is equivalent to the floating potential, and -100 V with a frequency of about 1550 Hz as can be seen in Fig. 4.2. By increasing the bias voltage, the power taken from the bias power supply and the voltage measured at the substrate holder becomes more uniform with less pronounced oscillations.

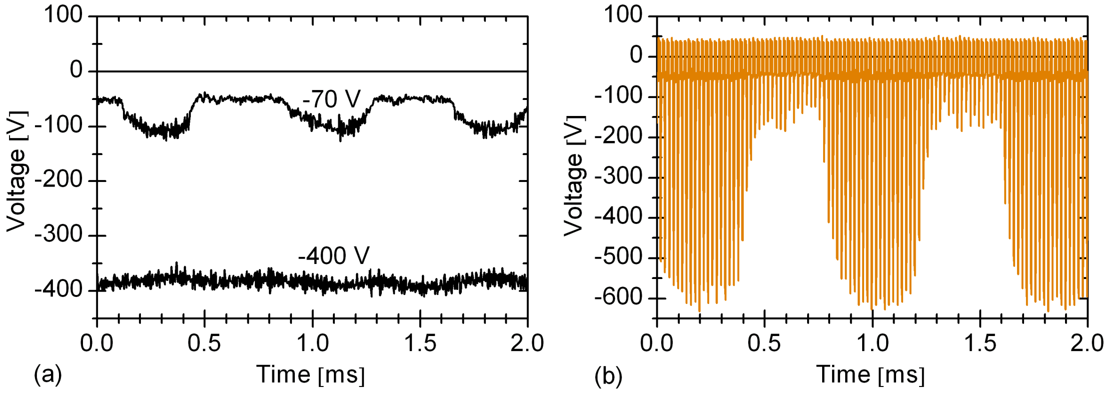

Fig. 4.2: Voltage measured at substrate holder for -70 V and -400 V in DC mode (a) and modulation of a 50 kHz pulse pattern (b).

In order to generate an asymmetric bipolar pulsed signal, the plasma generator utilizes two different integrated power units. The negative voltage is provided by the primary power unit, where a secondary low energy unit is used to achieve the positive pulse which is pre-set at +37 V. In order to reduce overload of the electric circuits and ensure a high line-to-output efficiency (> 85 %), the primary unit is kept switched-on during pulsing and the energy is temporarily stored in inductors. Such the application of frequencies from 50 up to 250 kHz with a positive pulse duration from a minimum of 496 ns up to a maximum of 40 % of one cycle (Fig. 4.3) is possible. However, when switching from the secondary to the primary unit, the stored energy is released into the system and causes a voltage overshooting. The magnitude of the overshooting is related to the energy stored in the inductors which depends on the duty cycle and the frequency. Figure 4.4 shows the voltage over time at 50 kHz with different duty cycles. In both cases the negative bias voltage is set at -70 V. The positive pulse levels off relatively fast (< 1 µs) and keeps

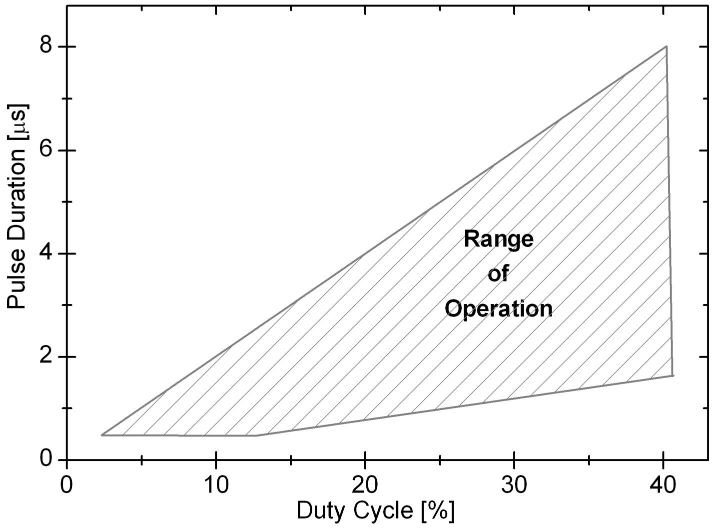

Fig. 4.3: Range of performance of the ENI RPG-50 generator.

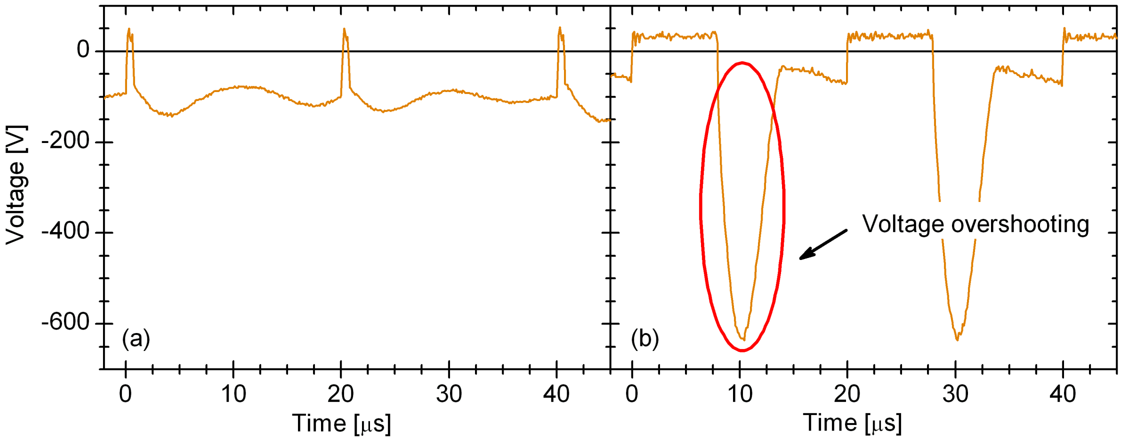

Fig. 4.4: Pulsed substrate bias voltage with a frequency of 50 kHz and duty cycle of 2.4 % (a) and 40 % (b), respectively. The circle indicates the voltage overshooting when switching from the secondary power unit to the primary power unit.

stable at approximately +37 V. After switching from the secondary to the primary power unit, the negative voltage can reach several hundreds volt depending on the chosen duty cycle. Moreover, a variation of the maximum of the voltage is shown due to variation of DC signal (Fig. 4.2).

It is known from previous measurements, that the Gencoa PP150 magnetron generates a uniform axial and radial distribution of the magnetic field lines [55, 56]. However, the homogeneous plasma distribution at the substrate holder is disturbed by the shutter used (Fig. 4.1), resulting in different ion-to-atom flux ratios at different locations of the substrate holder. These inhomogeneities cannot by measured successfully with conventional Langmuir probes due to additional disturbances of the plasma by the probe itself. It can be concluded that the arrangement of the shutter results in a lower ion-to-atom flux ratio in the area next to the shutter (due to loss of charge carriers at the grounded shutter in the closed position), while higher values can be expected further away. These different ion-to-atom flux ratios are denominated in the following as $J_{i-I}$ and $J_{i-II}$, where $J_{i-I} < J_{i-II}$.

The substrate bias voltage was recorded with a Tektronix TPS 2024 oscilloscope utilizing a PMK-PHV 1000 voltage probe.

### 4.1.2 Target, Substrate Materials and Working Gases

For the deposition of the coating, a pure metallic chromium target with a dimension ∅ 152.4 × 6 mm (Plansee Composite Materials GmbH) was used.

Coatings were deposited on silicon wafers in (100) orientation. 525 µm thick silicon wafers manufactured by Silchem were both sides polished and cut into pieces of 7 × 20 mm using a diamond scriber (ATV RV 126). The silicon substrates were intended for X-ray diffraction analysis, biaxial stress-temperature measurements, scanning electron microscopy, nanoindentation and profilometry experiments.

For reactive sputter deposition a mixture of argon and nitrogen working gases with a purity of 99.999 % were used.

### 4.1.3 Deposition Procedure

Prior deposition the samples were cleaned and degreased in successive supersonic baths in acetone and ethanol for 10 min. After mounting, the substrate holder was heated up to 350 °C to support degassing and desorption processes. The chamber was evacuated down to a base pressure of 4 × $10^{-3}$ Pa. As a next step in the deposition procedure, the substrate holder was cooled down to deposition temperature of 300 °C followed by sputter cleaning of the target for 10 min. For this purpose, the argon gas flow and the target current were set at 15 sccm and 1.5 A, respectively, yielding in a target power density of 3 $^{W}/_{cm^2}$. The shutter located in the front of the target was used in order to avoid substrate contamination during sputter cleaning. Sputter cleaning of the target was followed by ion etching of the substrates for 20 min. Next, the deposition of the coatings started where the target current was kept constant at 1.5 A. The gas flow of argon and nitrogen were adjusted to 11 and 5 sccm, respectively, yielding in a partial pressure ratio $^{p_{N_2}}/_{p_T}$ of 31 % and a total pressure of 0.4 Pa. The substrate bias voltage was varied between -70 and -400 V in DC mode. For coatings deposited with asymmetric bipolar pulsed substrate bias, the substrate bias voltage was set at -70 V while the frequency and the pulse duration were altered within the performance range of the bias generator. The substrate bias voltage characteristics was recorded by an oscilloscope during deposition. For the purpose of obtaining a coating thickness of approximately 3 µm, a deposition time of 60 min was chosen. In order to avoid contamination of the coating at elevated temperatures, the samples were cooled down to room under temperature vacuum conditions.

## 4.2 Coating Characterization

### 4.2.1 Optical Profilometry

The surface roughness of the coating shows a strong influence on the accuracy of surface sensitive measurements like nanoindentation or chemical analysis by energy-dispersive X-ray analysis. Furthermore, a change in surface roughness may indicate a change in the growth conditions of the CrN coating.

The surface roughness of the coatings was determined by a Vecco Instruments Wyko NT 1000 optical white light profiler. White light generated by an illuminator (1), is split up and reflected down to the objective (7) by a beam splitter (5), schematically shown in Fig. 4.5. A second beam splitter located in the Mirau Interferometer (8), and divides the light into two beams. One light beam is reflected from the sample surface, while the other light beam is reflected from a super smooth reference mirror. Both light beams recombine in the Mirau Interferometer. If the surface of the sample is in focus, interference patterns of light and dark bands are formed. The interference patterns are detected by the implemented CCD camera. The vertical position of each point is attained

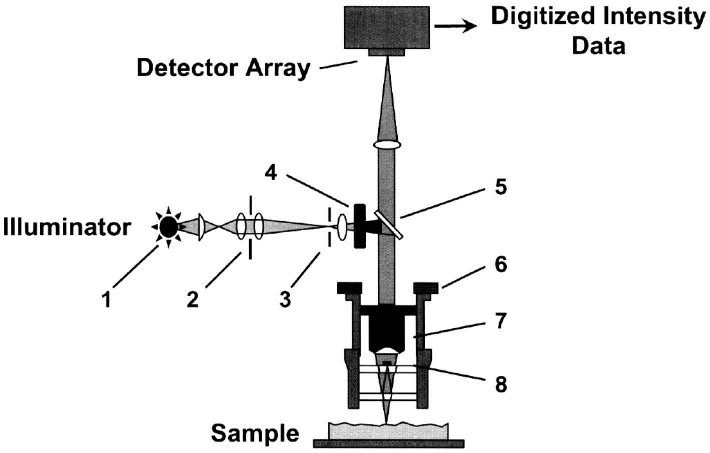

Fig. 4.5: Schematic representation of a white light profilometer. 1. . . Light source, 2. . . Aperture stop, 3. . . Field stop, 4. . . Filter, 5. . . Beam splitter, 6. . . Translator, 7. . . Microscope objective, 8. . . Mirau Interferometer.

by moving the objective (7) vertically and scanning the surface at varying heights. This mode is called vertical scanning interferometry (VSI) and allows a maximum scan length of 1 mm. Using the VSI mode a vertical resolution of 3 nm can be achieved [57, 58].

Originally, roughness statistics have been defined as two dimensional parameters. Those parameters have been adapted to measure tree dimensional surfaces, though their three dimensional usage was never standardized. In this work, the roughness average ($R_a$) was used for characterization of the coating surface. $R_a$ is useful for detecting general variations in overall profile height characteristics and is given in three dimensions by

$$R_a = \frac{1}{MN} \sum_{j=1}^{M} \sum_{i=1}^{N} |Z_{ji}| \,. \tag{4.1}$$

Here, $M$ and $N$ are the number of data points in the $X$ and $Y$ direction, respectively, of the array. The surface height to the reference mean plane is given by a parameter $Z$ [57, 58].

### 4.2.2 Coating Thickness Measurement

For certain measurement methods, for instance the determination of residual stresses, the knowledge of the thickness of the coating $t_c$ is required. Furthermore, the results of some mechanical testing methods like nanoindentation can be strongly influenced by $t_c$ as well as some characterization techniques, e. g. X-ray diffraction, electron-dispersive X-ray analysis (EDX) require a certain minimum material volume in order to give accurate

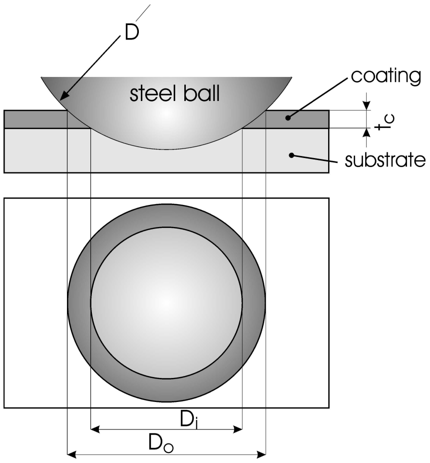

Fig. 4.6: Schematic of the ball crater technique.

results.

The ball crater technique is a very common method due to its quick and easy applicability in combination with a relatively good accuracy of 2-5 % for coating thicknesses in the order of $0.3 < t_c < 10\,\mu\text{m}$ [59]. In this technique a steel ball moistened with a liquid diamond suspension is used to grind a circular wear track into the coating surface as shown in Fig. 4.6. The inner $D_i$ and outer $D_o$ diameters of the circular wear track were measured by optical light microscopy with an attached CCD camera. Thus, the coating thickness can be derived using the simplified equation

$$t_c = \frac{D_o^2 - D_i^2}{8R}, \tag{4.2}$$

where $R$ designates the radius of the steel ball [60].

### 4.2.3 Scanning Electron Microscopy

The morphology and structure of fracture cross-sections of the coatings was investigated by scanning electron microscopy (SEM).

Elemental composition of the coatings were measured by energy-dispersive X-ray (EDX) emission spectroscopy and wavelength-dispersive X-ray (WDX) emission spectroscopy. Here, the surface of the sample is bombarded with electrons and consequently X-ray beams which are specific for the elements hit by the electrons are emitted. The X-ray beams are analyzed in terms of the energy and the wavelength, respectively. The intensity of the X-ray beams with a certain energy or wavelength correlates with the concentration of the element in the irradiated sample.

The samples were investigated by EDX due to its fast application. WDX was utilized in order to cross-check some measurements because it offers a higher resolution. The coatings were examined in the face of the $^{Cr}/_{N}$ ratio and in order to determine a possible contamination by incorporated Ar and $O_2$ due to the deposition process.

### 4.2.4 X-ray Diffraction Analysis

X-ray diffraction (XRD) analysis is a non-destructive characterization technique for phase determination of crystalline matters. Furthermore, structural properties such as grain size, coating texture or residual stress in the coating can be analyzed.

When a crystalline material is irradiated by electromagnetic radiation with a wavelength in the order of magnitude of the lattice dimension of the material, a characteristic diffraction pattern of a material is generated [61]. The correlation of the lattice spacing $d_{hkl}$, where h, k and l indicate the Miller indices, with the wavelength $\lambda_{X-ray}$ of the used radiation and the diffraction angle $\theta$ is called Bragg's law and can be written as

$$d_{hkl} = \frac{n\lambda_{X-ray}}{2\sin\theta}. \tag{4.3}$$

By comparison of the obtained diffraction patterns with the line positions $2\theta$ and relative line intensities of standards, e. g. from the International Centre for Diffraction Data (ICDD - also known as Joint Committee on Powder Diffraction Standards (JCPDS)) [62] the existing phases can be identified [63].

In this work phase analysis was done with a Bragg/Brentano Diffractometer (Siemens D500) as schematically shown in Fig. 4.7. In this geometry the sample surface is irradiated at an angle of $\theta$ and the diffracted X-ray beam is collected at an angle of $2\theta$ with respect to the incident beam. While the X-ray source is kept fixed the sample turns half the angular velocity of the detector and a so called $\theta$-$2\theta$-scan is obtained. By this geometry the lattice planes with the plane normal parallel to the diffraction vector are investigated. The main operating parameters are summarized in Table 4.1.

Tab. 4.1: Parameters for XRD measurements.

| $\lambda$ Cu $K_\alpha$ [Å] | $K_\beta$ Filter | High Voltage [kV] | Tube Curr. [A] | Step Time [s] | Step Size $2\theta$ [°] |
|---|---|---|---|---|---|
| 1.54056 | Ni | 40 | 30 | 1.2 | 0.02 |

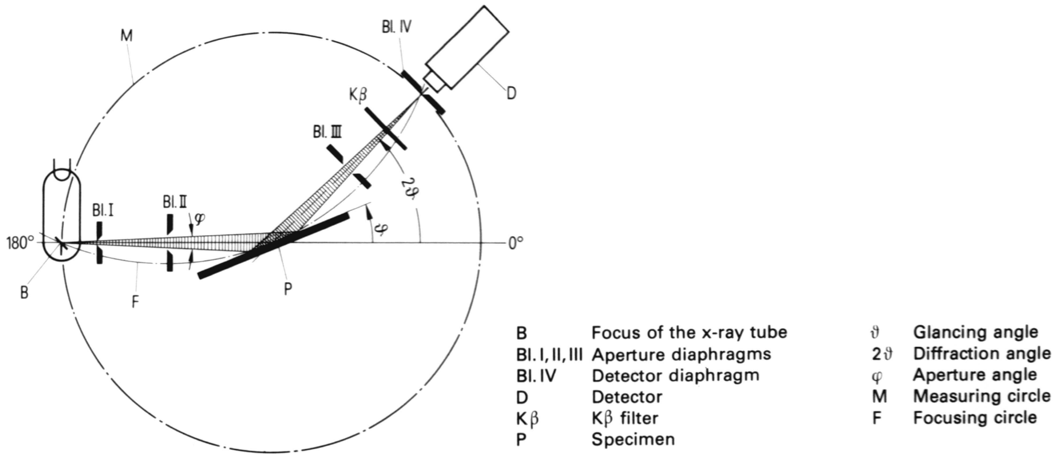

Fig. 4.7: Schematic of beam path in the Siemens D500 diffractometer with a $\theta$-$2\theta$ configuration. Aperture diaphragms (position I, II, III): 1°; Detector diaphragm (position IV): 0.15°; Diaphragm of diffracted beam monochromator: 0.6° [64].

Besides basic phase identification the obtained diffraction pattern also comprises additional information about the instrumental broadening as well as about the crystal structure of the sample. After elimination of the contribution of instrumental broadening, the grain size and the inhomogeneous strain can be determined by peak broadening analysis. A powerful single-line method is the application of the pseudo-Voigt function $f(x)$, where the measured profile is approximated by a linear combination of a Gaussian $f_{Gaussian}$ and a Cauchy (Lorentzian) $f_{Cauchy}$ function given by

$$f(x) = f_0 + A[\eta f_{Cauchy} + (1-\eta) f_{Gaussian}]. \tag{4.4}$$

Here, $f_0$ donates the mean background level, $A$ the peak area and $\eta$ the Cauchy component of the respective Voigt profile. It is assumed that the Gaussian component of the measured profile is solely due to strain. On the contrary, the Cauchy contribution arises due to crystallite size [65]. The Cauchy contribution must be greater than 0.328 in order to expect any meaningful accuracy in terms of data on crystallite size [66].

HARRIS [67] developed a method to quantify a preferred orientation of the coating by introduction of a texture coefficient $TC$. The texture coefficient is given by

$$TC_{(hkl)_i} = \frac{\frac{I_{(hkl)_i}}{I_{(hkl)_{i,0}}}}{\frac{1}{n_p}\sum_{j=1}^{n_p}\frac{I_{(hkl)_j}}{I_{(hkl)_{j,0}}}}, \tag{4.5}$$

where $TC_{(hkl)_i}$ is the texture coefficient of the peak $i$ indicated by the Millers indices $(hkl)$. $I_{(hkl)_i}$ and $I_{(hkl)_j}$ are the measured intensity of the peak $i$ and $j$, respectively. $I_{(hkl)_{i,0}}$ and $I_{(hkl)_{j,0}}$ are the corresponding intensities according to the ICDD powder diffraction files for the peak $i$ and $j$, respectively. The number of evaluated peaks of a sample is given by $n_p$. While $TC = 1$ for statistically distributed crystals, the texture coefficient of a sample with a preferred orientation can range from 0 to $n_p$. In order to compare texture coefficients calculated from a different number of evaluated peaks, the texture coefficient was modified by dividing $TC$ by the number of included peaks $n_p$ and is therefore named $TC'$. Such the sum of all modified texture coefficients $TC'$ of one investigated sample is always one instead of $n$.

### 4.2.5 Stress Measurement

Virtually all coatings deposited by physical vapor deposition processes exhibit a certain residual stress level $\sigma_{res}$. The residual stress level may be compressive or tensile in nature and refers to the internal stress distribution when all external boundaries of the system are free of applied traction [29]. It can approach the yield or fracture strength of the materials involved which may lead to a damage of the coating such as stress cracking, buckling or even delamination [4, 68, 69].

The residual stress is primarily composed of thermal $\sigma_{ther}$ and intrinsic $\sigma_{int}$ stress components:

$$\sigma_{res} = \sigma_{ther} + \sigma_{int}. \tag{4.6}$$

Here, the intrinsic stress may be caused by various effects in the coating itself, like contamination by impurities, the presence of defects as a consequence of a low energy ion bombardment during deposition and lower diffusion at lower deposition temperatures or occurrence of solid state transformations. The origin of thermal stress can be found in the coating/substrate interaction. Here, a mismatch in the coefficient of thermal expansion between the substrate and the coating, if deposited at elevated temperature and operated at a lower temperature, is the cause. The thermal stress can be written in a one-dimensional approximation as

$$\sigma_{ther} = -\frac{E_c}{1-\nu_c}(\alpha_c - \alpha_s)(T - T_s), \tag{4.7}$$

where $E_c$ is the Young's modulus and $\nu_c$ is the Possion's ratio of the coating, $\alpha_c$ and $\alpha_s$ are the linear thermal expansion coefficients of coating and substrate, and $T$ and $T_s$ are

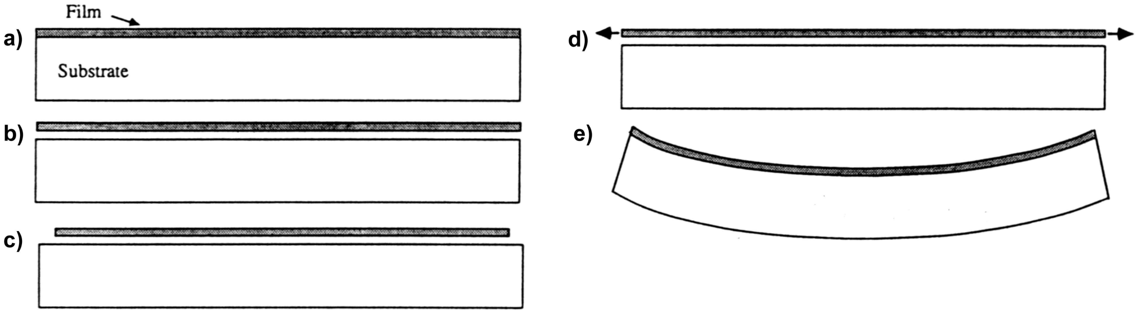

Fig. 4.8: Illustration of the relationship between biaxial stress in the coating and the associated bending of the substrate: Stress-free coating on the substrate (a); removal of the coating from the substrate (b); dimension changes of the coating relative to the substrate (c); imposing of stress to return coating to the substrate dimensions (d); reattachment of coating and removal of external forces (e) [70].

the temperature at which $\sigma_{ther}$ was measured and temperature of deposition, respectively [68].

Considering a coating/substrate composite that is completely free of stress (Fig. 4.8 a), it can be imagined to remove the coating from the substrate and allow it to stand in a stress-free state (Fig. 4.8 b). The lateral dimensions of the detached coating and the substrate match exactly. However, if the dimensions of the coating changes relatively to the substrate (Fig. 4.8 c), e. g. due to different thermal coefficients of the coating and substrate and changing temperatures, then the coating cannot be reattached. In this case tensile forces, causing biaxial stresses, must be imposed on the coating to elastically deform it and make the coating fit to the dimensions of the substrate again (Fig. 4.8 d). Considering these edge forces removed by superimposing forces of opposite signs on the edges of the coating, shear stresses on the coating/substrate interface arise. Such the biaxial stress is maintained in the coating and the substrate is caused to bend elastically (Fig. 4.8 e).

Analyzing the deformation of the coating/substrate composite requires to invoke a couple of assumptions which can be subsumed under the *thin film approximation*. For example, the thickness of the coating $t_c$ should be much smaller ($<100$ times) than the thickness of the substrate $t_s$ and the lateral dimension of the coating as well as the substrate ought to be much greater than their thicknesses [5, 29]. Under this approximation, the amount of bending caused by the biaxial stresses depends on the thickness and the biaxial Young's modulus of the substrate only. The relationship can be expressed by the simplified Stoney formula,

$$\sigma = \frac{E_s}{1-\nu_s}\frac{t_s^2}{6t_c}(\frac{1}{r}-\frac{1}{r_0}), \tag{4.8}$$

where $E_s$ designates the Young's modulus and $\nu_s$ the Poisson's ratio of the substrate, respectively and $r_0$ the initial radius of the curvature prior deposition [29].

In this work the residual stress was determined by the wafer curvature method which is an effective way of measuring the biaxial stress in a coating. Here, the curvature was assessed using two parallel laser beams and measuring the position of the reflected beams [70]. Figure 4.9 shows a schematic of the measurement setup which is described in detail in [71]. The measurement setup allows measurements of the curvature up to 700 °C under ambient conditions or in vacuum (base pressure of approx. $10^{-7}$ mbar). A laser source (Melles Griot Helium-Neon laser) emits a laser light having a wavelength $\lambda_{laser} = 632.8$ nm and a beam diameter of 1.2 mm. By utilization of a beam splitter, two laser beams with a parallel distance $d$ of 15 mm are generated. The two parallel laser beams are reflected from the backside of the coating/substrate composite. In order to increase the accuracy, a mirror is placed in the optical path and the laser beams are reflected back to the measuring plate. The deflection of the reflected beams $d'$ is measured and the curvature of the coating/substrate composite is calculated according

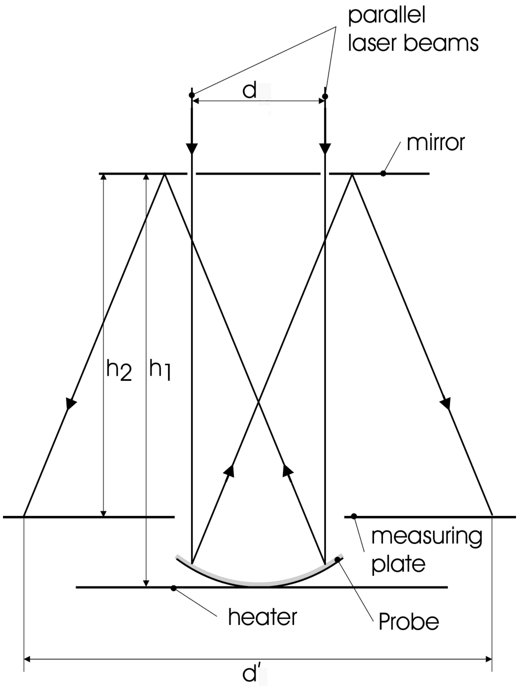

Fig. 4.9: Principle design of the stress measurement via two laser beams.

to:

$$r = \frac{2(h_1 + h_2)d}{d + d'}. \tag{4.9}$$

Here, $h_1$ and $h_2$ are the optical paths of the deflected laser beams and $d$ and $d'$ are the distances between the laser beams before and after reflection, respectively.

### 4.2.6 Hardness and Young's Modulus Evaluation

In materials science, the hardness $H$ of a solid material is usually defined as mechanical resistance against plastic deformation [4, 72]. It can be obtained, for instance, by pressing a specially shaped indenter into the surface and subsequent evaluation of the residual imprint. Such, the hardness is given by the ratio of the peak load $F_{max}$ to the residual projected area $A_p$ of the corresponding imprint according the equation

$$H = \frac{F_{max}}{A_p}. \tag{4.10}$$

Conventional hardness measurements are usually based on optical evaluation of the residual impression area after the indentation experiment. Here, a minimum load is required to generate a residual impression area big enough to allow an accurate optical evaluation in size of the imprint. On the other hand, in coatings the indentation depth has to be reduced to approximately 10 % of the coating thickness in order to avoid influences on the hardness measurement by the presence of a substrate. This limitation can be overcome by nanoindentation techniques which use the recorded depth of penetration of an indenter into the specimen along with the measured applied load to determine the area of contact [72, 73]. The applied force and the resulting penetration depth of the tip are continuously measured and recorded [74] and such a load displacement curve is gained (Fig. 4.10). The load-displacement curve is characteristic for the material and its mechanical properties, e. g. elastic modulus and hardness [75].

The initial penetration and the non-ideal geometry of the indenter were taken into account when the load-displacement curve was corrected. Using the method of Oliver and Pharr [76] the reduced Young's modulus can be derived from the slope of the unloading part of the load-displacement curve by

$$E_r = \frac{\sqrt{\pi}}{2C\sqrt{A_p}}. \tag{4.11}$$

Here, $C$ denotes the experimentally measured compliance of the system derived from of

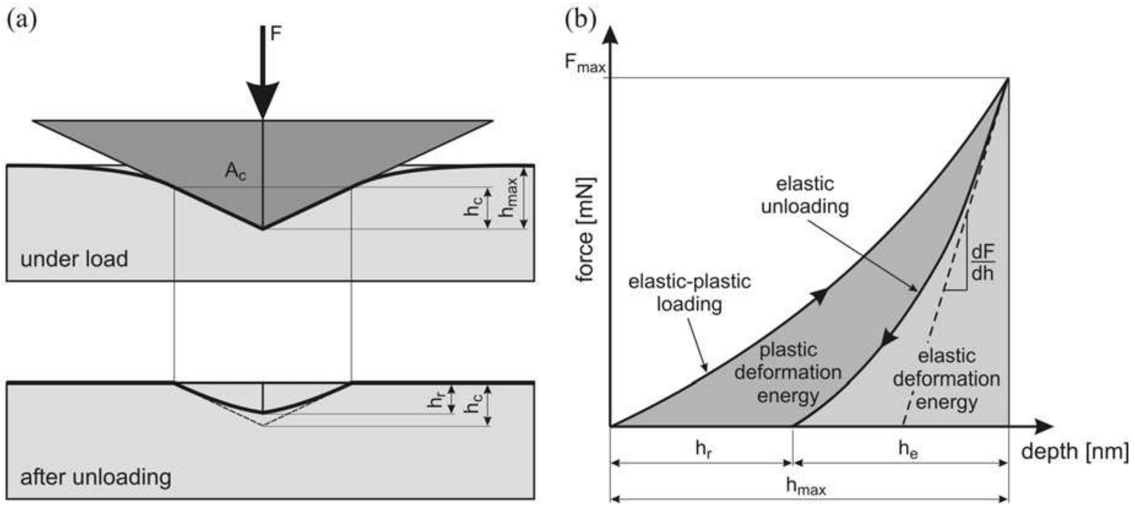

Fig. 4.10: Schematic representation through an indentation at full load and full unload for an elastic-plastic indentation (a). Load-displacement curve in a typical hardness experiment. In these experiments the contact stiffness ${}^{\mathrm{d}F}/_{\mathrm{d}h}$ at full load was determined by using a $2^{nd}$ degree polynomial fit to the upper 80 % of the unloading data (b).

the upper portion of the unloading data ${}^{\mathrm{d}F}/_{\mathrm{d}h} = C^{-1}$ and $A_p$ the projected contact area under peak load. The reduced Young's modulus $E_{red}$ can be calculated by

$$\frac{1}{E_{red}} = \frac{1-\nu_{mat}^2}{E_{mat}} + \frac{1-\nu_{ind}^2}{E_{ind}}, \tag{4.12}$$

where $E$ denotes the Young's modulus and $\nu$ the Poisson's ratio, the subscripts *mat* and *ind* refer to the investigated material and the indenter, respectively.

The nanoindenter used in the experiments, a CSIRO UMIS nanoindentation system is equipped with a Berkovich indenter. The indenter tip is made of diamond and possesses a face angle of 65.3° which gives the same projected area-to-depth ratio as a Vickers indenter. Experience shows that, compared to the more familiar Vickers indenter, a sharper tip and therefore a higher accuracy is possible with a Berkovich indenter [73, 77]. The indenter and the linear variable differential transformers for depth and force are situated in the measurement head. Such, a depth range of either 2 and 20 µm and a load range of either 50 and 500 mN can be chosen. Both, the measurement head and the sample positioning stage are attached on a heavy gray cast iron construction which acts as seismic mass. The sample positioning stage is controlled by a closed loop linear servo motion control enabling a step size of 0.1 µm both in X and Y directions. The samples are hot mounted onto cylindrical hardened steel specimen mount which are magnetically held on the sample positioning stage [78]. In order to further reduce mechanical vibrations, originating from the surrounding, the UMIS nanoindentation system is placed on a pneumatic shock absorber system. By this setup a depth resolution of 0.003 µm and load resolution of 0.05 µm is achievable, respectively.

# 5 Results and Discussion

## 5.1 Phase Analysis

X-ray diffraction experiments were performed on CrN coatings deposited on silicon single crystal (111) substrates in $\theta$-$2\theta$ mode. The detected reflections have been compared to diffraction data of unstressed bulk CrN reference material (ICDD card no. 01-077-0047) and silicon (00-027-1402), respectively. Qualitative X-ray analysis shows fcc CrN phase structure of a NaCl-type only. No $Cr_2N$ was detected, revealing single phase structure of the coatings. A peak shift to lower $2\theta$ angles, corresponding to larger lattice spacing, could be detected for all displayed CrN reflections, whereas the substrate peaks match their reference positions. The coatings were deposited with different ion-to-atom $^{J_i}/_{J_a}$ flux ratios with $J_{i-I}$ and $J_{i-II}$, where $J_{i-I} < J_{i-II}$.

### Results – unpulsed

The effect of the energy and flux of the impinging particles on the CrN microstructure was investigated in a wide range of substrate bias of -70 to -400 V (Fig. 5.1). In the case of low ion flux $J_{i-I}$ and bias voltage of -70 V, a main diffraction peak ($TC'$ of approx. 0.7) was observed at a $2\theta$ value of 63 °, which corresponds to the (220) orientation (Fig. 5.1 a). Other reflections correspond to (311), (200) and (111) oriented grains having a texture coefficient between 0.22 and 0.04. With increasing $V_b$ a significant change in texture was observed. At $V_b =$ -200 V the (220) peak becomes less pronounced while the (200) peak dominates ($TC'$ of approx. 0.9). Further increase of $V_b$ to -300 and -400 V leads to a texture change where the (200) peak diminishes and (220) is the only remaining peak having a texture coefficient of 0.7 and 0.9, respectively. CrN coatings grown at high ion flux $J_{i-II}$ (Fig. 5.1 b) revealed a (220)-dominated structure when a bias voltage of -70 V was applied. With higher bias voltage ($V_b =$ -200 V), the (220) and (200) peaks become more pronounced. If a critical bias voltage value of -200 V is exceeded, the intensity of the CrN peaks is drastically reduced – low intense (111) and (220) can be found, whereas a single (220) peak remains only at $V_b =$ -400 V. A minor increase of peak deviation to lower $2\theta$ angles could be detected for both ion-to-atom flux ratios.

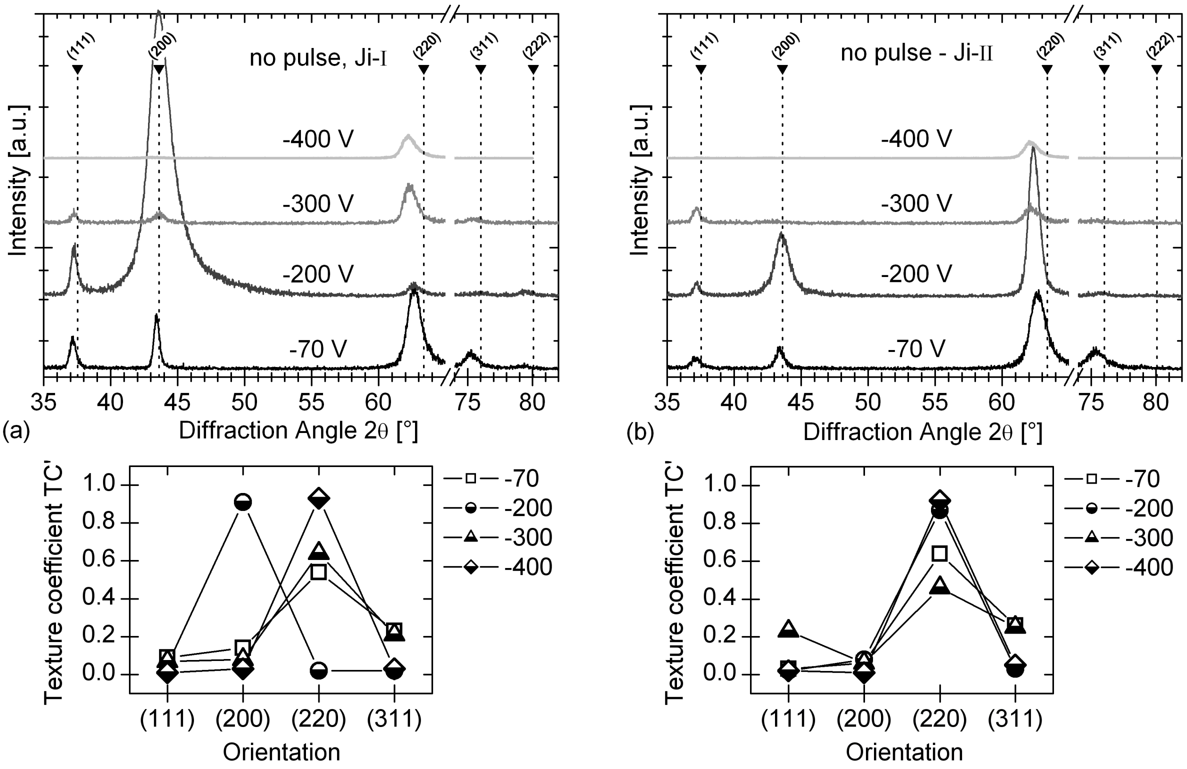

Fig. 5.1: X-ray diffractions patterns and texture coefficient ($TC'$) from CrN coatings deposited on silicon as a function of different DC bias voltages (-70, -200, -300 and -400 V) and ion-to-atom ratios (${}^{J_i}/_{J_a}$): $J_{i-I}$ (a) and $J_{i-II}$ (b).

## Discussion – unpulsed

It is often found that sputter deposited coatings develop a preferential crystallographic orientation different from bulk reference material formed under equilibrium conditions. Usually, this is caused by the different growth rates of certain crystal planes [79]. In order to understand the evolution of texture, a simple approach based on energy considerations is very common [79]. In general, the crystal as a system tends to minimize its total energy. Hence, texture can be considered as a result of the competition of mainly two contributing energies.

The *free surface energy* varies with the considered family of lattice planes. A schematic of the unit cell of a NaCl (B1) structure which is typical for CrN in thermal equilibrium at temperatures above 285 K is shown in Fig. 5.2 a. Here, applying a simple bond breaking model shows that (100) planes have the lowest surface energies and, consequently, the lowest adatom diffusivity causing the highest average adatom residence time [36, 79–82]. *Strain energy* can be induced due to imperfections of the crystal (like voids or atoms on interstitial lattice sites) caused typically by energetic particle bombardment.

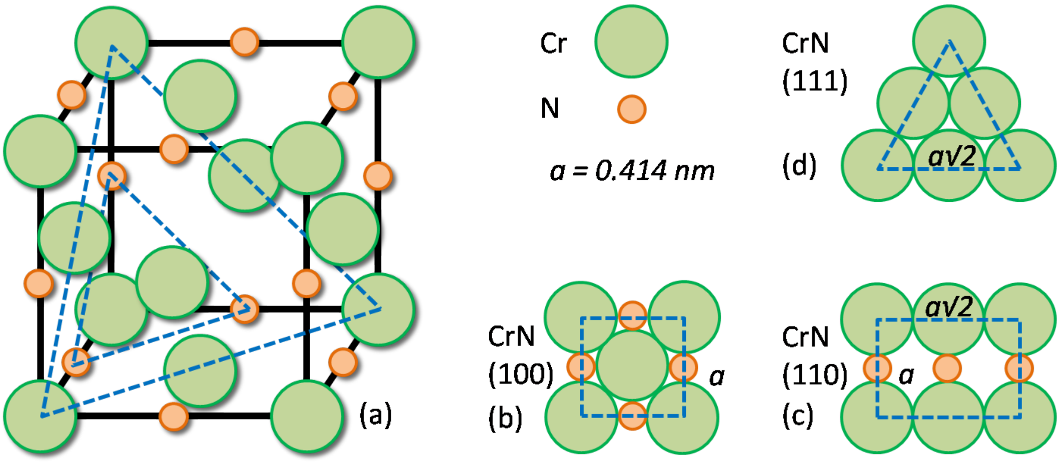

Fig. 5.2: Scheme of the NaCl (B1) structure (a) with distinguished lattice planes (100) (b), (110) (c) and (111) (d).

Another effect is described as macroscopic stress caused by a different lattice spacing of coating and substrate material [29]. For the CrN NaCl (B1) type microstructure, the (111) orientation is the plane with the lowest strain energy due to the anisotropy in Young's modulus of different lattice directions. Therefore its alignment perpendicular to the growth direction would decrease the total energy under strain dominated growth. The level of strain energy usually rises with increasing film thickness and results in a texture change.

Nevertheless, additional factors contributing to the texture should be considered: (i) Reactive gas covering the surface also changes the mobility of adatoms. On (111) lattice planes atomic nitrogen tends to bind chromium forming CrN, whereas at (100) planes the formation of molecular nitrogen and subsequent desorption is more likely. Both processes are highly sensitive to the amount of excess nitrogen available on the surface. (ii) Energetic particle bombardment favors the more densely packed crystallographic planes (100) to be formed parallel to the impinging direction [4]. (iii) Channeling of argon is less hindered along [100] and [110] directions, thus re-sputtering of (100) and (110) lattice planes is reduced at higher ion-energies [38, 83]. (iv) A given orientation of the substrate like in the case of single-crystal silicon, may also stimulate the growth of certain lattice directions.

The main parameter affecting the growth of the CrN coatings within the present experiments was the state of ion bombardment expressed by ion energy (via $V_b$) and amount of impinging energetic particles (via $^{J_i}/_{J_a}$). Considering a plasma potential ($V_p$) as measured to approximately 45 V, the minimum ion energy $E_i$ was in the range of about 25 eV, since $E_i = e(V_b - V_p)$, where $V_b$ is the applied bias voltage. Whereas low ion energies lead to (220) texture, a higher ion energy favors the (200) orientation. Ion energies higher than 175 eV result in switching back of the preferred texture to (220) indicating the surpassing of a threshold energy responsible for the evolution of the (220) lattice planes. The lack of (111) might be related to the heavy ion bombardment causing a non-thermodynamically controlled growth, rather channeling effects might be attributed to the findings. A higher amount of impinging particles ($J_{i-II}$) results in amplified perturbations of the growth process and no cross-over in texture could be found – (220) lattice planes dominate all XRD diffractograms. In both cases, the intensity of the measured peaks diminished at high ion energies. The dominating (220) orientation at higher bias voltages corresponds to results reported by Hurkmans *et al.* [51, 84], however contradicts findings published by Tischler [55] and Chekour *et at.* [85].

### Results – pulsed bias

The effect of pulsed bias voltage with a base bias voltage of -70 V in combination with various frequencies and pulse durations is shown in Figs. 5.3–5.5. First, the influence

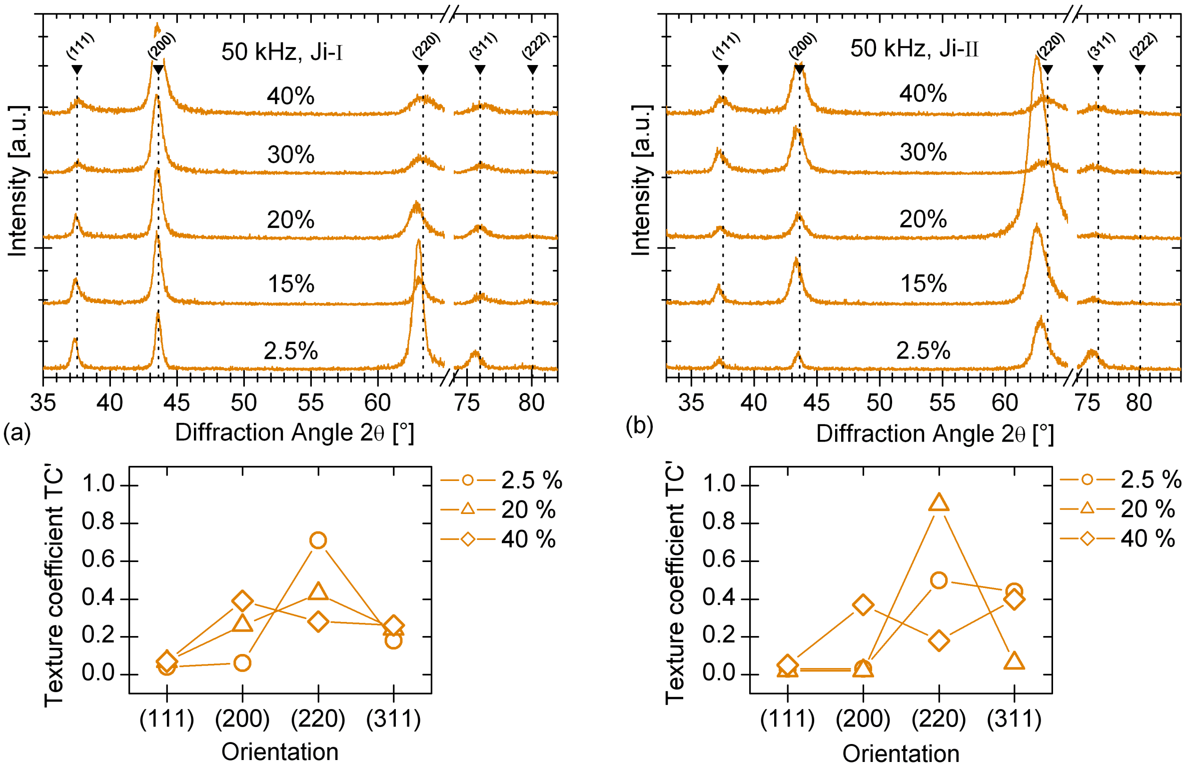

Fig. 5.3: XRD patterns and texture coefficient of samples coated at $V_b$ = -70 V with constant frequency (50 kHz) and different duty cycles (2.5, 15, 20, 30 and 40 %) with $J_{i-I}$ (a) and $J_{i-II}$ (b).

of 50 kHz pulses with duty cycles between 2.5 and 40 % is displayed. For low ion flux ($J_{i-I}$) and low duty cycle (2.5 %) the (220) peak is the most dominant having a $TC'$ higher than 0.7 (Fig. 5.3 a). This peak diminishes with increasing duty cycle, whereas (200) becomes the most intensive reflection. A higher ion flux induces the formation of the (220) peak for duty cycles between 2.5 and 20 %. Whereas the $TC'$ of the (220) reflection reaches a maximum of 0.9 at 20 %, higher duty cycles promote a change in texture towards (200) and $TC'$ of (220) drops below 0.15. For both ion-to-atom flux ratios, the (111) reflection never reaches the intensity typical of undistorted CrN bulk reference material.

As next, XRD patterns of CrN coatings grown with constant pulse duration ($\tau = 0.5$ µs) as a function of the frequency and $J_i/J_a$ are plotted in Fig. 5.4. X-ray diffractograms show

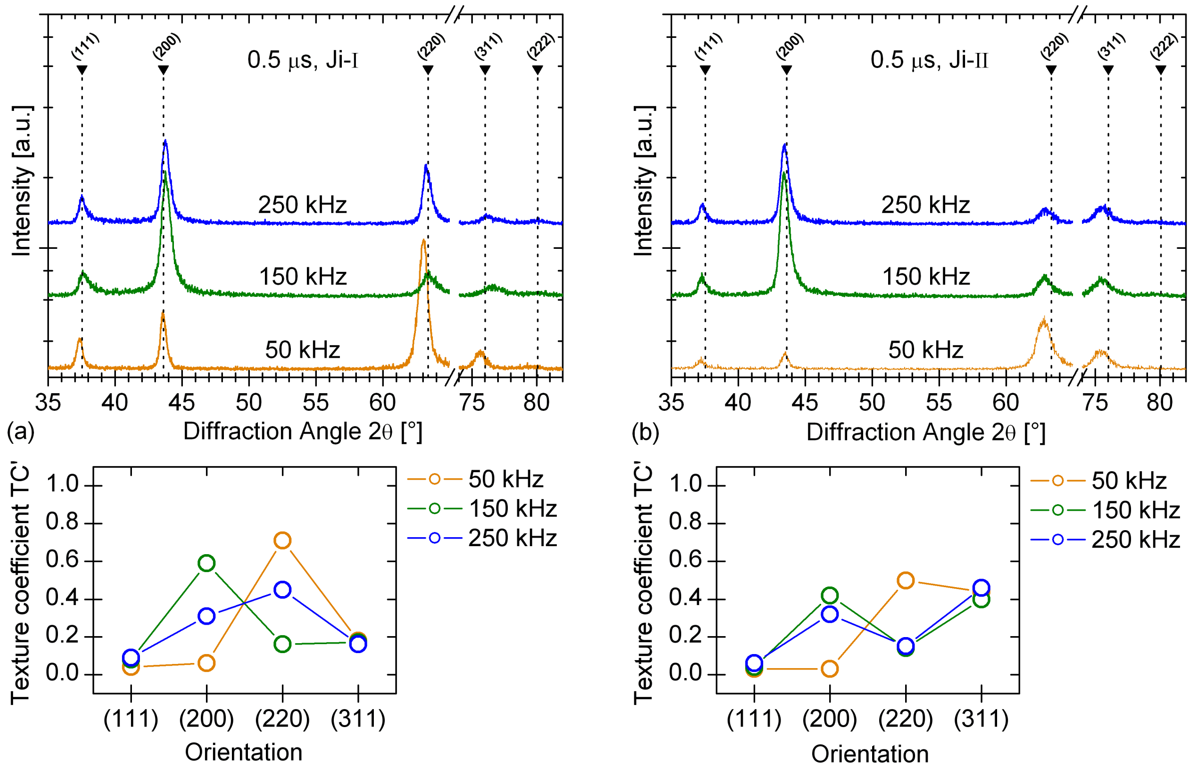

Fig. 5.4: XRD patterns and texture coefficient of samples coated at $V_b$ = -70 V with constant pulse duration (0.5 µs) and different frequencies (50, 150 and 250 kHz) with $J_{i-I}$ (a) and $J_{i-II}$ (b).

the (220) peak as most intensive at low frequency value (50 kHz). A cross-over in texture from (220) towards (200) accompanied by a drop in $TC'$ of (220) from 0.7 to 0.25 can be detected at frequencies higher than 50 kHz. The change in the preferred orientation is more pronounced for higher ion-to-atom flux ratio ($J_{i-II}$).

Finally, Fig. 5.5 displays the effect of pulse frequency on the preferred orientation for low and high ion-to-atom flux ratios. All diffractograms are dominated by the (200)-reflection. The texture coefficient for the (200) reflection is in range of 0.5 to 0.7. All other peaks show a $TC'$ between 0.1 and 0.2 (not shown here). Neither a variation of the frequency value nor in ion-to-atom ratio suggests a significant impact on the texture.

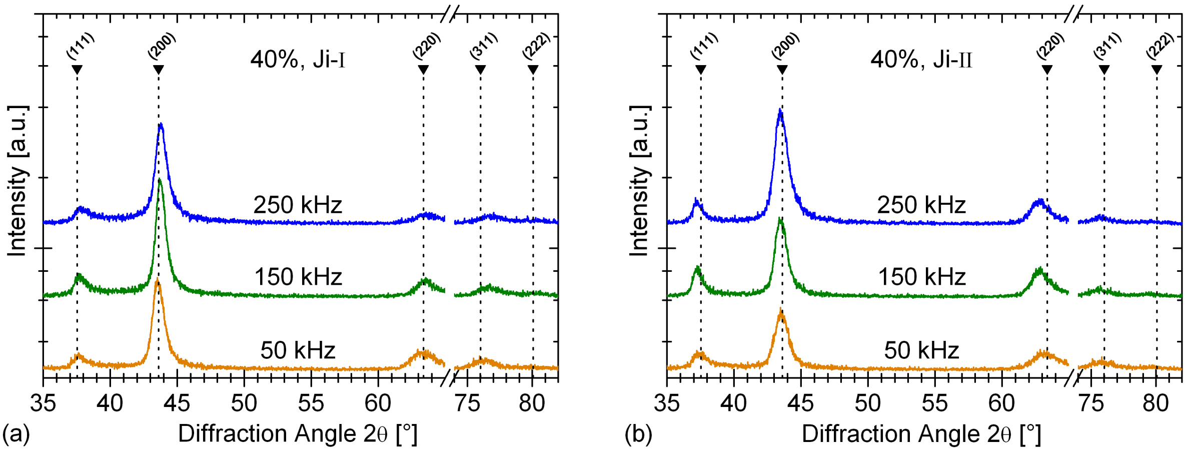

Fig. 5.5: XRD patterns of samples coated at $V_b$ = -70 V with duty cycle = 40 % and different frequencies (50, 150 and 250 kHz) with $J_{i-I}$ (a) and $J_{i-II}$ (b).

## Discussion – pulsed bias

For low duty cycles (2.5 %), the XRD diffractograms reveal a similarity to XRD patterns of unpulsed CrN coatings shown above (Fig. 5.1), suggesting the same growth mechanisms dominating. At higher duty cycles, growth conditions are in favor of lowering the surface energy, hence the (200) peak develops and becomes the preferred orientation of planes parallel to coating surface. A higher duty cycle means an additional short but high energetic ion bombardment due to the overshooting as well as longer plasma based electron bombardment (PBEB) of the coating. The energy of the impinging energetic particles reaches a maximum at 40 % with peak voltages of more than 600 V. This is a consequence of the design of the plasma generator ENI RPG-50 originally designed to drive a magnetron in PVD processes. Due to intrinsic features of the generator, a negative overshooting of the voltage is introduced after each positive oscillation as explained in chapter 4 and shown in Fig. 5.6. The peak voltage caused by the voltage overshooting may reach a multitude of the selected base bias voltage. The magnitude of the voltage peak depends primarily on the selected frequency and duty cycle (Fig. 5.7). At the same time, the duration of PBEB is extended to up to 40 % of the overall deposition time causing an energy input into the coating surface and surface near region without

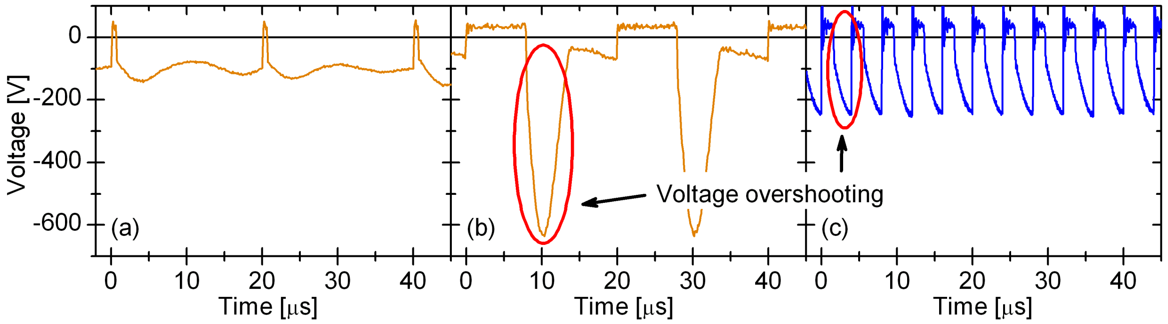

Fig. 5.6: Characteristic bias voltage shown for 3 different pulse parameters: 50 kHz at 2.5 % (a) and 40 % (b) as well as 250 kHz at 40 % (c).

the destructive effect of high energetic ion bombardment. However, the annealing effect of PBEB is not strong enough to induce a significant change in texture towards (111) which is typical for elevated deposition temperatures (higher than 400 °C) as reported by GAUTIER *et al.* [86]. In the case of a higher amount in impinging particles ($J_{i-II}$), the cross-over in texture from (220) to (200) orientation occurs first at a duty cycle of 20 %.

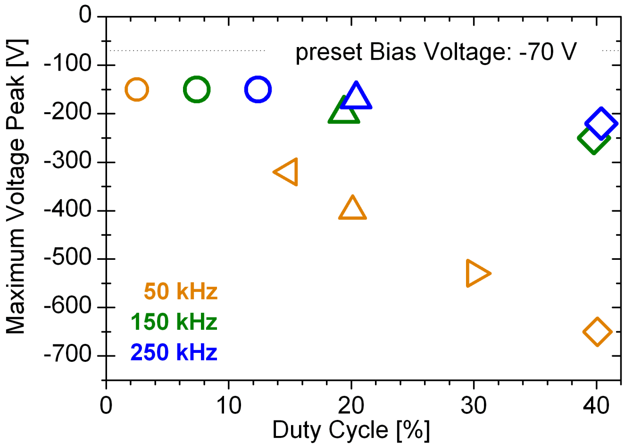

Fig. 5.7: Maximum overshooting of the bias voltage in relationship to the pulse frequency and duty cycle.

In the case of constant pulse duration (Fig. 5.4), the increase in frequency corresponds to an increase in duty cycle from 2.5 up to 12.5 for 50 and 250 kHz, respectively. The influence on the peak voltage and therefore on the ion energy due to increased duty cycle is negligible as can be seen in Fig. 5.7. Hence, the change in texture can be related to the amount of impinging ions as well as the overall time of the PBEB which are both five times higher for a frequency of 250 than for 50 kHz, respectively. The difference in the ion-to-atom flux ratio shows no distinct influence in the cross-over of the preferred texture from (220) towards (200). This is probably due to two concurrent processes, namely the ion bombardment and the PBEB. Basically, both processes increase the adatom mobility. However, the impact of ion bombardment on the microstructure depends very much on the energy of the impinging particles. Here, the effects encompass surface densification as well as grain refinement due to re-nucleation and even amorphization at very high energy levels of the ions, thus indicating the complexity of the growth process.

For the same reasons, a variation of the frequency at DC bias base voltage (-70 V) and constant duty cycle (40 %) as shown in Fig. 5.5 does not show any significant effect onto the microstructure of the CrN coating. The complex interplay of evolved parameters shows a stable growth condition favoring the evolution of (200) orientation.

## 5.2 Chemical Composition

The chemical composition of CrN coatings in as-deposited state was measured by energy dispersive X-ray (EDX) spectroscopy. The $^{Cr}/_{N}$ ratio of CrN coatings deposited with high ion flux ($J_{i-II}$) on silicon substrates (Fig. 5.8 b) was found to be roughly 1 (within the limits of detection). It indicates a stoichiometric composition of the CrN layers. Samples

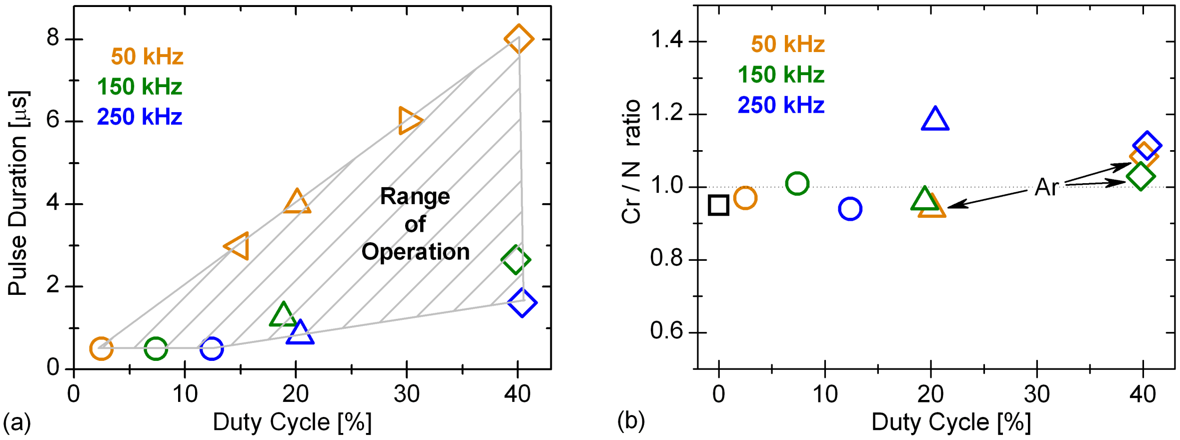

Fig. 5.8: Range of operation of the bias generator with investigated pulse parameters (a). Chemical analysis of the $^{Cr}/_{N}$ ratio by EDX (b). Samples with traces of Ar are indicated by arrows.

deposited on pulsed biased substrates, featuring a high overshooting of the bias voltage, showed small amount of argon incorporated in the coating during deposition process ((Fig. 5.8 b – marked by arrows). In order to determine a possible contamination of CrN coatings by oxygen from the residual atmosphere, WDX analysis was conducted as well. The results revealed no traces of oxygen in the coatings, however confirmed the presence of argon.

The probability of argon ions accelerated in the cathode sheath region to be incorporated in the CrN coatings is increasing with their energy. In our experiments the ions can reach an energy higher than 600 eV. In combination with the channeling effect of certain lattice directions ([100] and [110]), a deep penetration into the coatings can be expected [38, 83]. Both conditions were fulfilled in the case of the samples containing argon. In order to illustrate the effect of energetic particle bombardment on the noble gas incorporation, additional SRIM/TRIM simulations were performed.

### SRIM/TRIM simulation

The Stopping and Range of Ions in Matters / The Transport of Ions in Matters (SRIM/ TRIM) software package has been developed by Ziegler [87–89]. The software is a group of programs by which the stopping power, range straggling, damage distribution and sputtering yield of particles can be simulated over an energy range between 10 eV and 2 GeV. The simulation is based on a quantum-mechanical treatment of ion-atom collisions utilizing the binary collision approximation (BCA). In order to simplify the notation, the moving species (Ar) are called ions and the target species (Cr and N) are called atoms. Here, the movement of ions in the target is treated as a succession of individual collisions between recoil ion and atoms in the sample. For each individual collision the classical scattering integral is solved by numerical integration.

Figure 5.9 shows the results of a TRIM-2008 simulation for two different ion energies (70 and 650 eV). The ordinate gives the number of argon in a certain depth ($^{\text{atoms}}/_{\text{cm}}$).

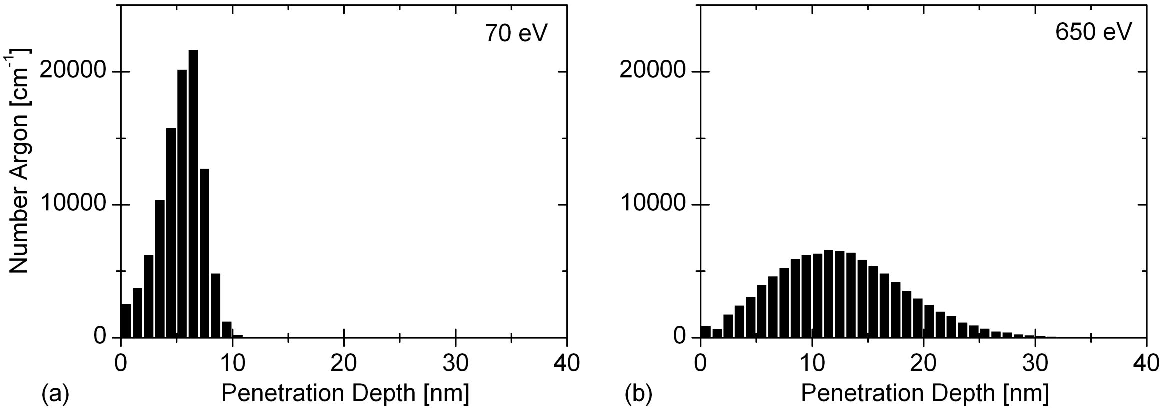

Fig. 5.9: TRIM-2008 simulation of the distribution of argon in CrN for ion energies of 70 eV (a) and 650 eV(b).

The argon density ($^{\text{atoms}}/_{\text{cm}^3}$) in the target (coating) is gained by multiplication of the number of argon by the ion dose or so called fluence ($^{\text{atoms}}/_{\text{cm}^2}$). Simulation was performed by calculating 100 000 Ar-ions incident perpendicular at the surface of the CrN coating with an energy of 70 and 650 eV, respectively. The density was set at 6.12 $^{\text{g}}/_{\text{cm}^3}$ [90], all other parameters were taken as suggested by the code.

Penetration of particles having lower energies is restricted mainly to the near surface region with a average depth of penetration of less than 10 nm. Ions with a higher energy (650 eV) achieve a much higher penetration of depth into the CrN coating of 12 nm in average with a maximum penetration depth of more than 25 nm. However, the distribution of the ions in the target is more shallow as the ions undergo more collisions with atoms (Fig. 5.9).

The accuracy of the results is restricted by two major simplifications specific to the code. These are the zero dose assumption meaning that previous ions have no effect on subsequent ions and that the target temperature is 0 K and therefore no thermal effects like thermal diffusion or thermal annealing occur. Furthermore, it should be noted that no absolute data can be obtained due to lack of accurate data on lattice, surface and binding energies of chromium nitride. At last, one should notice that the ion energies used for TRIM-2008 simulations and bias voltage cannot be directly compared, as the plasma sheath in the process is certainly collisional (p = 0.4 Pa). Hence, only qualitative statements can be retrieved. In order to deduce quantitative results, a cross-check with experimental methods, e. g. elastic recoil detection analysis (ERDA) is recommended as shown in [91].

## 5.3 Morphology and Coating Thickness

The morphology of the CrN coatings deposited with the higher ion-to-atom flux ratio ($J_{i-II}$) was investigated by means of scanning electron microscopy (SEM) and white light profilometry. The pseudo-Voigt analysis of the XRD spectra was utilized in order to estimate the grain size. Coating thickness was derived form cross-section scanning electron micrographs and by using the ball-crater technique.

### Scanning electron microscopy

SEM was performed on fresh broken cross-sections of CrN coatings grown on single crystal silicon. Typical scanning electron micrographs of the coatings deposited with both, DC and pulsed bias (50 and 250 kHz) are depicted in Figs. 5.10 – 5.12, respectively.

The SEM image of the CrN coatings deposited at DC bias voltage of -70 V, as shown

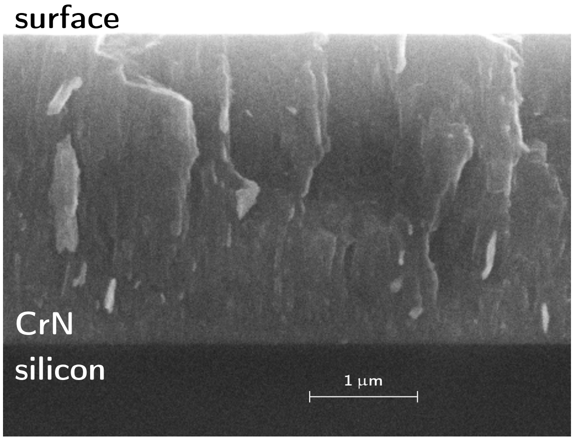

Fig. 5.10: Scanning electron fracture micrograph of CrN coating deposited on silicon with DC substrate bias voltage of -70 V.

in Fig. 5.10, reveals the influence on morphology, densification and surface roughness on the 3 µm thick CrN coating The image of the cross-sections shows a smooth and almost structureless morphology. The surface roughness is very smooth corresponding to an average surface roughness of several nm. Both fractures are typical for nearly stoichiometric CrN coatings deposited by reactive UBM sputtering [84].

SEM observations of the fractured cross-sections of CrN coatings deposited with pulsed bias (50 kHz) and two different duty cycles (2.5 and 40 %) are shown in Fig. 5.11. In the case of a low duty cycle (2.5 %), a dense and fine grained structure can be seen near to the substrate-coating interface, indicating a very high number of nuclei per unit of area. In contrast, as the coating thickness increases during growth, a cross-over into a dense microstructure featuring V-shaped columns can be observed. The dense

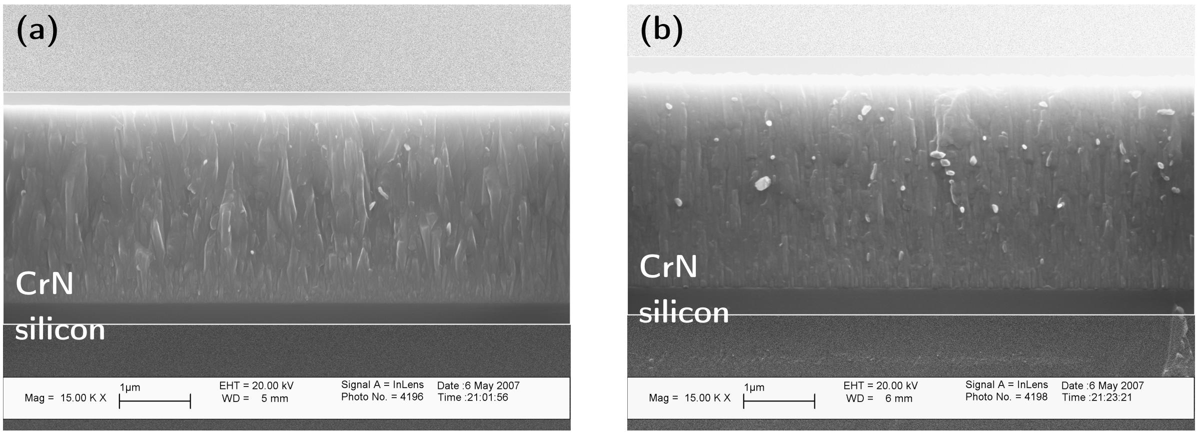

Fig. 5.11: Cross-section SEM image of CrN coatings deposited onto silicon with pulsed bias of 50 kHz and duty cycles of 2.5 % (a) and 40 % (b), respectively.

and columnar microstructure corresponds to Zone T growth typical for CrN coatings deposited at elevated temperatures with concurrent ion bombardment [92]. At higher duty cycle (40 % – Fig. 5.11 b), the scanning electron micrograph exhibits a similar fine grained zone near the interface as shown before, whereas the columnar structure becomes less pronounced with increased distance from the interface compared to Fig. 5.11 a. The grain refinement is probably caused by increased re-nucleation due to more intense ion bombardment at higher duty cycles induced by the amplified overshooting of the DC bias generator. No signs of interface cracks or peeling were found after fracture which indicates that the coatings adhere well to the silicon.

Examination by SEM of cross-sections of CrN coatings grown at higher frequency (250 kHz) but different duty cycles (12.5 and 40 %) revealed an overall dense, columnar structure (Fig. 5.12). Both images show a fully dense and fine-grained zone next to the substrate-coating interface which is related to a high density of nucleation sites. During growth, again, a decrease in the nucleation density was found and a transition to a fully dense microstructure featuring V-shaped columns occurs. At higher ion-to-atom flux ratio ($J_{i-II}$), a pronounced growth of columns is inhibited and a dense but structureless fracture cross-section of the CrN coating was obtained. Both micrographs show an unscathed substrate-coating interface revealing a good adhesion of CrN on silicon.

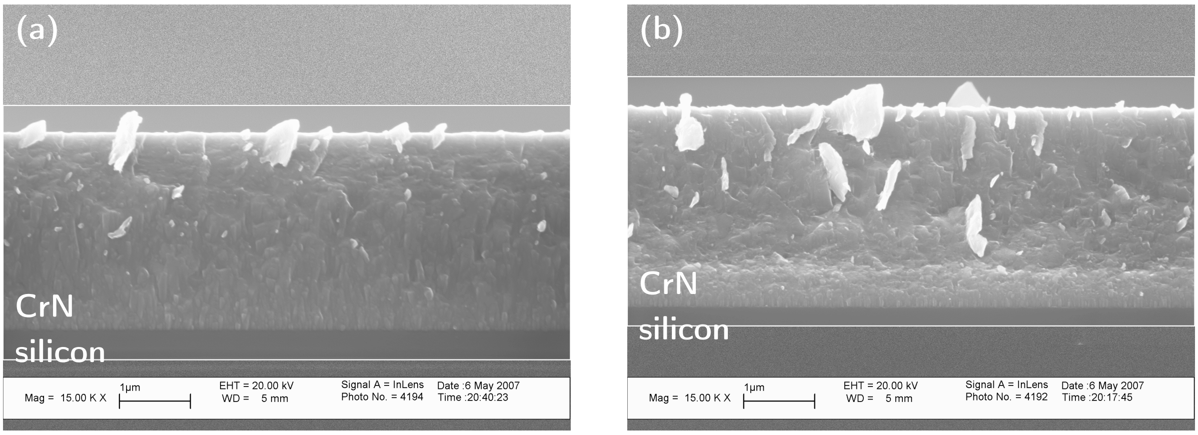

Fig. 5.12: Cross-section SEM image of CrN coatings deposited onto silicon with pulsed bias of 250 kHz and duty cycles of 12.5 % (a) and 40 % (b), respectively.

It can be seen that the microstructure becomes more fine-grained and even structureless with increasing pulse frequency and/or duty cycle. This is caused by the more intensive ion bombardment at higher duty cycles due to the overshooting as well as the shorter time interval between the more energetic ion bombardment at higher frequencies. At the same time surface defects caused by the ion bombardment are counterbalanced by annealing effects due to the more intensive PBEB at higher duty cycles leading to a very smooth surface and morphology of the coating.

### Coating thickness

Determination of the CrN coating thickness by evaluation of SEM images and Calo-wear testing revealed a uniform thickness of 2.8 µm for all CrN coatings deposited with pulsed bias. These contradicts results reported by KELLY *et al.* [93] describing a reduced growth rate at least at higher duty cycles due to increased re-sputtering caused by high energetic particle bombardment. In our case the re-sputtering is not dominant and does not lead a thickness reduction, while the deposition time is kept constant.

### Grain size

The grain size of CrN coatings grown with pulsed bias (Figs. 5.3 – 5.5) was derived from single-line analysis of (111), (200), (220) and (311)-peaks in the XRD patterns. Results of the numerical analysis of the X-ray patterns using the pseudo-Voigt profile function [65, 66] are shown in Fig. 5.13 – 5.14. At first, the influence of duty cycle on the basis of CrN coatings deposited with 50 kHz is shown (Fig. 5.13). In the case of lower $^{J_i}/_{J_a}$ the average crystallite size is in the range of 20 nm and decreases with increasing duty cycle down to 5 nm. A higher ion-to-atom flux ratio ($J_{i-II}$) reduces the average grain size to 10 nm in average. Here, the duty cycle reveals no distinct influence.

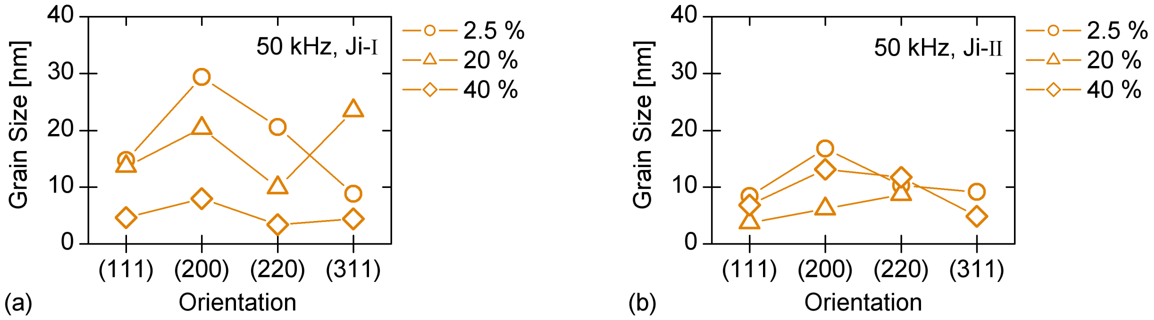

Fig. 5.13: Grain size of samples coated at $V_b$ = -70 V with constant frequency = 50 kHz and different duty cycles (2.5, 20 and 40 %) with $J_{i-I}$ (a) and $J_{i-II}$ (b).

Next, the dependency of various frequencies at constant pulse duration upon the grain size is shown in Fig. 5.14. A reduction in grain size can be determined with increasing frequency at low $^{J_i}/_{J_a}$, which complies with SEM micrographs shown before (Fig. 5.11 and 5.12). The grains size reduces from 20 nm at 50 kHz to 10 nm at 250 kHz. No such trend is visible in the case of high ion-to-atom flux ratio, where the grain size is 15 nm in average.

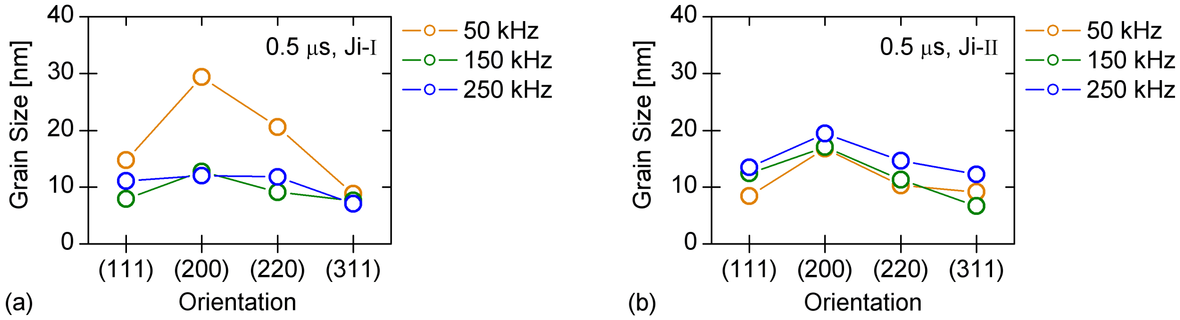

Fig. 5.14: Grain size of samples coated at $V_b$ = -70 V with constant pulse duration (0.5 µs) and different frequencies (50, 150 and 250 kHz) with $J_{i-I}$ (a) and $J_{i-II}$ (b).

Figure 5.15 depicts the grain size of CrN coatings grown with different frequencies at constant duty cycle in relation to the measured orientations. Here, no distinct influence of the duty cycle on the crystallite size of the CrN coatings can be observed. Single line analysis of the X-ray diffractograms reveals a grain size in the range of 5 to 10 nm.

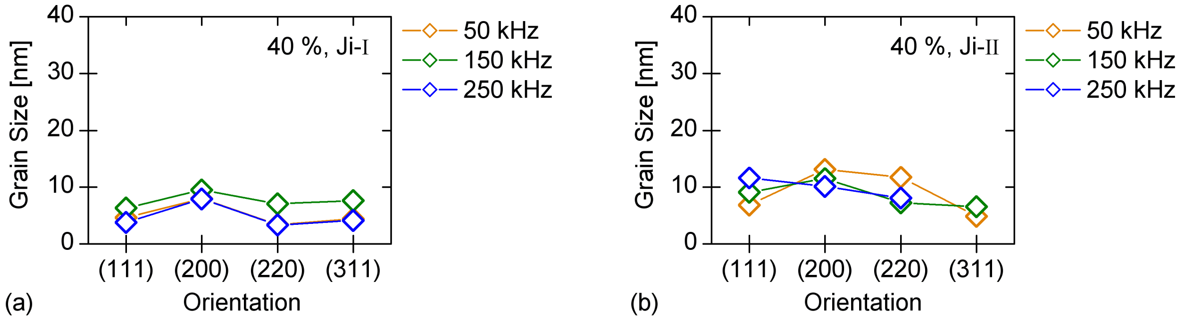

Fig. 5.15: Grain size of samples coated at $V_b$ = -70 V with constant duty cycle (40 %) and different frequencies (50, 150 and 250 kHz) with $J_{i-I}$ (a) and $J_{i-II}$ (b).

In general, the results of the pseudo-Voigt analysis (5 to 30 nm) correspond well with values typically found in literature for CrN coatings grown by reactive UBM sputtering [20, 50, 55, 94–96]. However, it must be noted, that the application of the pseudo-Voigt analysis on XRD pattern is constricted to a minimum grain size which is in the area of about 10 nm. For grain sizes below this limit no reliable deduction can be made.

### Surface roughness

The average surface roughness, $Ra$, of the CrN coatings was below the limit of detection of the utilized white light profiler. Hence, the maximum average surface roughness must be in the order of 3 nm or less.

In the formation of the coating surface two concurrent processes are involved. On one hand it is supposed that enhanced surface mobility of adatoms encourages the development of a smooth surfaces, e. g. due to elevated substrate temperature caused by substrate heating or PBEB as well as soft ion bombardment induced surface mobility. On the other hand, an intensive ion bombardment generates many surface defects, thus roughening the coating surface [97]. In our case the ion bombardment is either not intensive enough to cause severe surface defects (Fig. 5.10) or smoothening processes induced by PBEB outbalance the negative effect of high energy ion impact due to the overshooting voltage (Fig. 5.11, 5.12).

## 5.4 Biaxial Residual Stress

The residual stress ($\sigma_{res}$) of as-deposited CrN coatings grown on both, DC and pulsed biased silicon substrate was determined at room temperature by the wave-curvature method. In general, all as-deposited CrN coatings are in the state of residual compressive stress.

### Results

The development of the residual stress in the CrN coating in the as-deposited state with increasing bias voltage (-70 to -400 V) is displayed in Fig. 5.16.

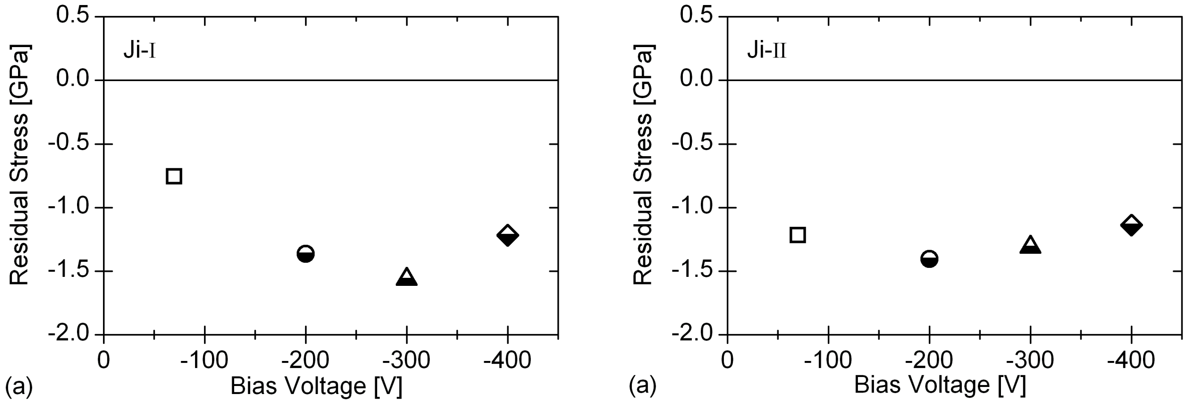

Fig. 5.16: Residual stress in CrN coatings deposited with DC bias voltages of $V_b = -70$ to -400 V with $J_{i-I}$ (a) and $J_{i-II}$ (b).

In the case of low ion-to-atom flux ratio ($J_{i-I}$), $\sigma_{res}$ in CrN coatings grown at $V_b = -70$ V is about -0.8 GPa. Increasing bias voltage leads to higher compressive stress levels, reaching a maximum at -300 V of -1.6 GPa followed by a reduction in residual stress down to -1.2 GPa at -400 V as can be seen in Fig. 5.16 a. CrN coatings deposited with higher $J_i/J_a$ reveal a higher residual stress level at low voltages (-1.2 GPa at -70 V) followed by a slight increase reaching a maximum stress level at -200 V of almost -1.5 GPa. Further increase results in a steady decrease down to -1.1 GPa at $V_b$ = -400 V in the residual stress level of the as-deposited CrN coatings (Fig. 5.16 b).

Residual stresses as a function of pulsed bias voltage with a base bias voltage of -70 V and various combinations of pulse frequencies as well as duty cycles in 2.8 µm thick CrN coatings are depicted in Fig. 5.17. $\sigma_{res}$ of coatings grown with low frequency, pulse length and ion-to-atom flux ratio (50 kHz, 0.5 µs and $J_{i-I}$) is about -0.7 GPa, which is almost the same as in CrN coatings deposited on DC biased substrates ($V_b$ = -70 V). An increase in frequency and/or duty cycle reduces the residual stress, resulting in stress values in the range of -0.1 to -0.4 GPa. Again, in the case of low frequency and pulse length (50 kHz and 0.5 µs), CrN coatings deposited with $J_{i-II}$ exhibit almost the same residual stress as deposited on DC biased substrates ($V_b$ = -70 V), which is about -1.3 GPa. Up to duty cycles of 20 %, $\sigma_{res}$ is in the order of -1.5 GPa, independent of the applied frequency. At high duty cycles (40 %) all coatings are in a lower state of stress, in the case of a deposition with 50 kHz a residual stress level of close to zero was measured.

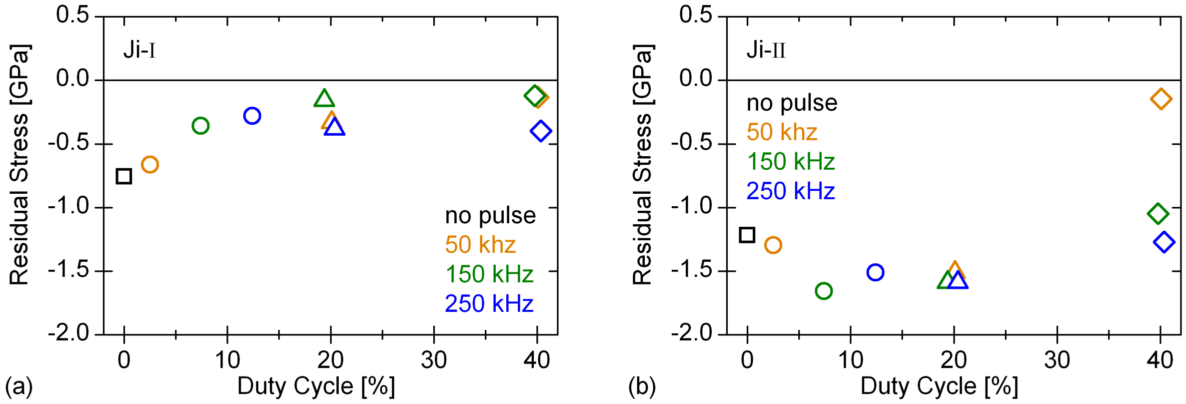

Fig. 5.17: Residual stress in CrN coatings deposited with pulsed bias at $V_b$ = -70 V with different frequencies and duty cycles (50 – 250 kHz and 2.5 – 40 %) with $J_{i-I}$ (a) and $J_{i-II}$ (b).

## Discussion

The residual stress of PVD coatings can be divided into two broad categories: (i) Externally induced stresses and (ii) stresses caused by the growth of the coating on substrates [29, 68]. The latter, commonly called intrinsic stress, is strongly affected by ion peening, originally denoted by D'HEURLE in 1970 as *shot-peening* [98]. The resulting impact of the ion peening on the microstructure and hence in the stress generation is closely related to the energy of the ions. For very low energetic ions, such as encountered in sputtering processes with substrates kept at floating potential, large numbers of voids in combination with low levels of compressive or even tensile stress are often found [84, 99]. Coatings of transition metal nitrides (e. g. TiN, CrN) grown by reactive UBM sputter processes with concurrent ion bombardment exhibit usually a denser structure and higher stress level up to several GPa in the as-deposited state [84, 100]. Here, the energetic particles which impinge on the surface during deposition may be incorporated well below the surface as, for example, shown for argon ions in the TRIM-2008 simulation above (Fig. 5.9). The incorporation of energetic ions is accompanied by momentum transfer between the incident particles and bulk lattice atoms, resulting in the displacement of the latter and thus creating point or cluster defects. Consequently, the lattice is strained and corresponding fields of stress are induced. This is in good agreement with our experiments for bias voltages in the range up to -300 and -200 V in the case of low and high ion-to-atom flux ratio, respectively. The decrease of $\sigma_{res}$ at higher DC bias voltages might be related to stress relieve effects, as reported in literature [99]. Both, CrN coatings grown at -70 V DC bias and pulsed bias with low frequencies in combination with a low duty cycle are in the same state of stress. This can be expected due to the fact that almost no overshooting as well as very little PBEB is generated at low duty cycles (Fig. 5.18 b). On the contrary, increased frequencies as well as duty cycles exhibit

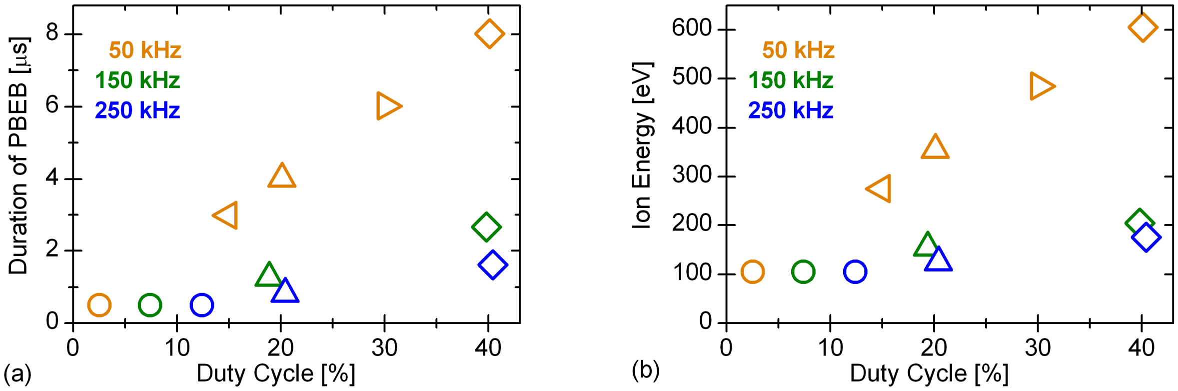

Fig. 5.18: Duration of PBEB (a) and ion energy (b) as function of the duty cycle.

a distinct influence on the residual stress level. At low $J_i/J_a$ the enhanced adatom mobility and thus the increased annealing effect of PBEB outbalances the void and defect generation caused by ion bombardment. Whereas, high numbers of impinging ions as in the case of $J_{i-II}$ significantly contribute to the compressive stress level in the CrN coating and exceed the stress relieving influence of PBEB. However, at high duty cycles of 40 %, corresponding to high ion energies of approx. 650 eV (Fig. 5.18 b), the compressive stress is reduced. This is probably caused by the stress relieve effects reported for high energized ions as described above, thus, reflecting the complexity of growth processes under reactive atmosphere and bombarding conditions [29, 69, 84, 85, 92, 98–100].

## 5.5 Hardness

The hardness was measured by nanoindentation techniques using a Berkovich-type indenter. Maximum load was kept constant at 35 mN for 1 s, resulting in indentation depths in the range of 250 to 300 nm. For each set of deposition conditions the average and the standard deviation of at least 16 indentations is shown.

### Results

The hardness values of as-deposited CrN coatings are presented in Fig. 5.19 as a function of the duty cycle. Figure 5.19 a shows the hardness of CrN coatings deposited with low ion flux ($J_{i-I}$). The hardness is in the range of 16 to 17 GPa independent of the applied duty cycle during deposition. The nanoindentation of CrN coatings grown with higher ion-to-atom ratio ($J_{i-I}$) shows in average a higher hardness (Fig. 5.19 b). Here, the pulsed biasing with low frequencies results in decreasing hardness values with increasing duty cycle. At low duty cycle (2.5 %) a hardness of 18 GPa was measured, whereas at high duty cycle of 40 % the hardness values of about 15 GPa were obtained. This effect is less pronounced in the case of a frequency of 150 kHz and disappears at higher frequencies (250 kHz), where the hardness values are constantly in the range of 20 GPa.

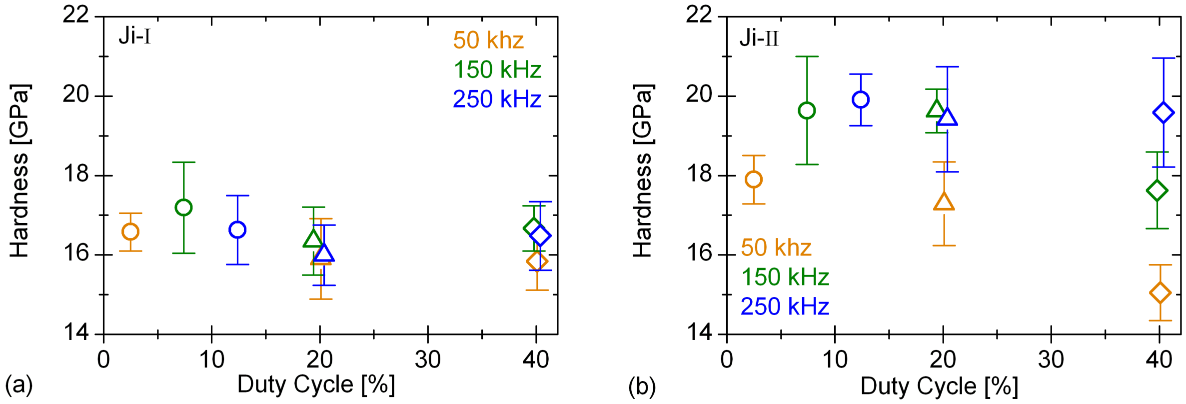

Fig. 5.19: Hardness of CrN coatings deposited with pulsed bias at $V_b = $-70 V with different frequencies and duty cycles (50 – 250 kHz and 2.5 – 40 %) with $J_{i-I}$ (a) and $J_{i-II}$ (b).

### Discussion

For bulk chromium nitride a hardness value of around 11 GPa is reported [90]. In our experiments, the hardness values of sputter deposited CrN coatings vary from 15 to 21 GPa which is similar to values obtained by other authors [53, 84, 86, 94, 101, 102]. The difference in coating hardness and bulk hardness of chromium nitride can be explained by the compressive stress in coatings as well as a fine grain hardening mechanism according the Hall-Petch relationship [70].

The dependency of hardness and residual stress of the CrN coatings upon the duty cycle and the frequency exhibit an evident resemblance, which point to a mutual relation between those two quantities. The interrelationship between residual stress and hardness is shown in Fig. 5.20. Here, a low level of residual compressive stress corresponds to lower values in hardness and vice versa, independently of the ion-to-atom flux ratio. Both, residual stress and hardness in coatings are closely related to the density of lattice defects (e. g. interstitial atoms, voids, Frenkel pairs) [20]. The higher the number of lattice defects in general, the higher is the fields of stress. Similarly, a high number of obstacles straining the lattice and causing stress-fields is acting as strong barrier against dislocation movement. Consequently, the resistance to plastic deformation is increased, corresponding to a higher hardness of the solid material [11].

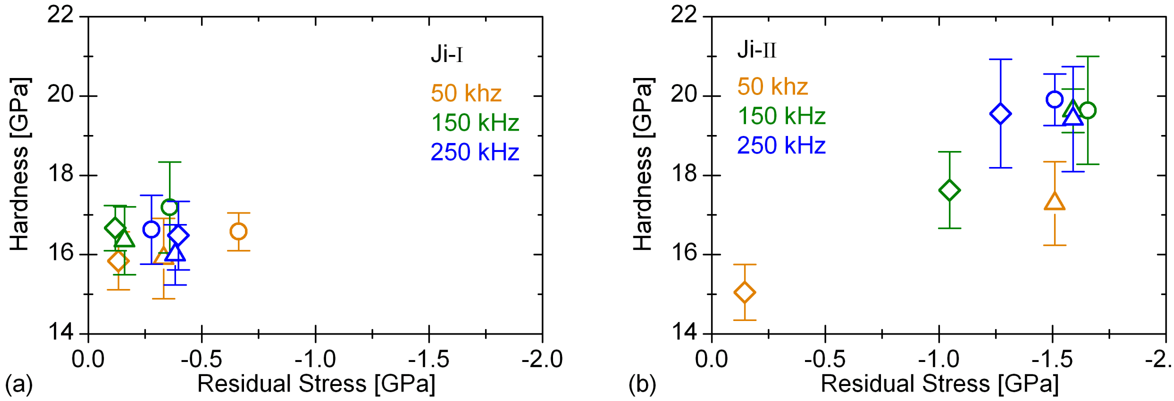

Fig. 5.20: Interrelationship between hardness and residual stress of CrN coatings deposited with different frequencies and duty cycles (50 – 250 kHz and 2.5 – 40 %) with $J_{i-I}$ (a) and $J_{i-II}$ (b).

# 6 Summary and Conclusions

Within this work, the beneficial effect of plasma based electron bombardment (PBEB) and ion bombardment in various quantities on the microstructure and mechanical properties of the CrN coatings was studied. Therefore, CrN coatings were deposited by reactive unbalanced magnetron sputtering on silicon substrates. The PBEB and ion bombardment was controlled by means of an ENI RPG-50 power supply connected to the substrate holder. With this setup, DC as well as asymmetric bipolar pulsed bias voltages were applied. Due to special features of the bias power supply setup, the intensity of the PBEB is reflected by the pulse duration only, whereas the ion bombardment is also influenced by the frequency. Here, it should be noted that the lower the frequency and the longer the pulse duration is, the more energetic the ion bombardment becomes.

The application of a low frequency in combination with short pulse durations exhibits no significant differences to coatings deposited with DC bias, independently of $^{J_i}/_{J_a}$. However, with increasing frequency and/or pulse duration, two cases can be distinguished depending on the ion-to-atom flux ratio.

In the case of low ion-to-atom flux ratio, the PBEB induced annealing effects outbalance the effect of ion bombardment with increasing frequency and pulse duration. This results in lower residual stress levels and concordantly lower hardness values of the CrN coatings.

The deposition of CrN coatings with higher frequency and/or longer pulse duration as well as an increased number of impinging ions, given by $^{J_i}/_{J_a}$, consequences the domination of the ion bombardment. Hence, the residual stress levels as well as the hardness values of the CrN coatings remain at a high level. However, very long pulse durations yield lower residual stress levels and hardness values probably evoked by high energetic ion bombardment causing additional stress relieving effects as mentioned in [99].

Independently of $^{J_i}/_{J_a}$ an increasing PBEB and ion bombardment changes the microstructure of the investigated CrN coatings from a dense V-shaped columnar growth towards a fully dense and very fine grained microstructure, as observed by scanning electron microscopy. The observed decrease in grain size with increasing frequency and/or ion bombardment was verified by pseudo-Voigt analysis of X-ray patterns. These effects are probably caused by the intensified re-nucleation due to the higher number in lattice defects acting as nucleation sites. The very smooth coating surface as observed by white light profilometry can be related to PBEB and ion bombardment enhanced adatom mobility.

Low frequencies in combination with long pulse durations, which refers to a high energetic ion bombardment, caused the incorporation of argon into the CrN lattice, as detected by wavelength dispersive X-ray analysis. This is due by the overshooting effect of the bias power supply leading to high acceleration voltages near the substrate surface. SRIM/TRIM simulations confirm the greater penetration depth of heavy particles facing high acceleration voltages.

Finally, it can be concluded that PBEB in combination with ion bombardment is a versatile instrument with the possibility of taking targeted influence on the microstructure and hence the mechanical properties of coatings deposited by PVD.

# Nomenclature

## Constants, Symbols (greek, roman) & Abbreviations

### Constants

| | |
|---|---|
| $\epsilon_0$ | permittivity of free space … $8.854\,187 \times 10^{-12}\ \mathrm{C^2/Nm^2}$ |
| $k_B$ | Boltzmann's constant … $8.617\,342 \times 10^{-5}\ \mathrm{eV/K}$ |
| $m_e$ | electron mass … $9.109\,381 \times 10^{-31}\ \mathrm{kg}$ |

### Symbols – greek

| | |
|---|---|
| $\alpha$ | degree of ionization |
| $\alpha_c$ | linear thermal expansion coefficient of the coating |
| $\alpha_s$ | linear thermal expansion coefficient of the substrate |
| $\eta$ | Cauchy content of $f(x)$ |
| $\theta$ | incident angle of the X-ray beam on the substrate |
| $\lambda_D$ | Debye length |
| $\lambda_{laser}$ | wavelength of laser light |
| $\lambda_{X-ray}$ | wavelength of the X-ray source |
| $\nu_c$ | Poisson's ratio of the coating |
| $\nu_{ind}$ | Poisson's ratio of the indenter |
| $\nu_{mat}$ | Poisson's ratio of the material |
| $\nu_s$ | Poisson's ratio of the substrate |
| $\sigma_{int}$ | intrinsic stress |
| $\sigma_{res}$ | residual stress |
| $\sigma_{ther}$ | thermal stress |
| $\tau$ | pulse duration |
| $\omega_p$ | plasma frequency |

### Symbols – roman

| | |
|---|---|
| $A$ | peak area of $f(x)$ |
| $A_p$ | projected area after indentation |

| | |
|---|---|
| $\vec{B}$ | magnetic field |
| $C = {}^{\mathrm{d}h}/_{\mathrm{d}F}$ | compliance |
| $d$ | distance between laser beams |
| $D$ | duty cycle |
| $d_{hkl}$ | lattice spacing for planes with $hkl$ |
| $D_i$ | inner diameter |
| $D_o$ | outer diameter |
| $\vec{E}$ | electric field |
| $E_{av}$ | average energy of particles |
| $E_c$ | Young's modulus of the coating |
| $E_{ind}$ | Young's modulus of the indenter |
| $E_i$ | ion energy |
| $E_{mat}$ | Young's modulus of the material |
| $E_{red}$ | reduced Young's modulus |
| $E_s$ | Young's modulus of the substrate |
| $f(x)$ | pseudo-Voigt profile |
| $f_{Cauchy}$ | Cauchy (Lorentzian) function |
| $f_{Gaussian}$ | Gaussian function |
| $F_{max}$ | peak load during intendation |
| $H$ | hardness |
| $hkl$ | Miller indices |
| $I_{hkl}$ | measured intensity of the peak with the $hkl$ |
| $M, N$ | number of data points |
| $n$ | charger carrier density |
| $n_e$ | number of electrons |
| $n_i$ | number of ions |
| $n_p$ | number of evaluated peaks |
| $R$ | radius of steel ball |
| $r_0$ | initial radius of curvature prior deposition |
| $T$ | periode |
| $t_c$ | coating thickness |
| $TC$ | texture coefficient |
| $TC'$ | modified texture coefficient |
| $T_e$ | electron temperature |
| $T_m$ | coating material melting point |

| | |
|---|---|
| $T_s/T_m$ | homologous temperature |
| $T_p$ | plasma temperature |
| $t_s$ | substrate thickness |
| $T_s$ | coating temperature during deposition |
| $V_b$ | bias voltage |
| $V_f$ | floating potential |
| $V_p$ | plasma potential |
| $X, Y, Z$ | directions |

## Abbreviations

| | |
|---|---|
| at.-% | atomic percent |
| bcc | body-centered cubic |
| e. g. | *exempli grati* – for example |
| fcc | face-centered cubic |
| i. e. | *id est* – that means |
| sccm | standard cubic centimeters per minute |

| | |
|---|---|
| BCA | binary collision assumption |
| CBM | conventional balanced magnetron |
| CCD | charge-coupled device |
| DC | direct current |
| EDX | energy-dispersive X-ray analysis |
| ERDA | elastic recoil detection analysis |
| ICCD | International Centre for Diffraction Data |
| JCPDS | Joint Committee on Powder Diffraction Standards |
| PBEB | plasma based electron bombardment |
| PVD | physical vapor deposition |
| SEM | scanning electron microscopy |
| SRIM | The Stopping and Range of Ions in Matter |
| SZM | structure zone model |
| TRIM | The Transport of Ions in Matter |
| UBM | unbalanced magnetron |
| Vol.-% | volume percent |
| VSI | vertical scanning interferometry |
| WDX | wavelength-dispersive X-ray analysis |
| XRD | X-ray diffraction analysis |

# List of Figures

# Bibliography

[1] J.T.M. de Hosson and A. Cavaleiro. Galileo comes to the Surface! In A. Cavaleiro and J.T.M. de Hosson, editors, *Nanostructured Coatings*. Springer, Berlin, 2006.

[2] W. Tillmann and E. Vogli. Selecting Surface-treatment Technologies. In F.-W. Bach, A. Laarmann, and T. Wenz, editors, *Modern Surface Technology*. WILEY-VCH, Weinheim, 2006.

[3] K. Bobzin, E. Lugscheider, M. Maes, and P. Immich. Innovations in PVD Technology for high-performance Applications. In F.-W. Bach, A. Laarmann, and T. Wenz, editors, *Modern Surface Technology*. WILEY-VCH, Weinheim, 2006.

[4] D.M. Mattox. *Handbook of Physical Vapor Deposition (PVD) Processing*. Noyes Publications, New Jersey, 1998.

[5] M. Ohring. *Materials Science of Thin Films - Deposition and Structure*. Academic Press, San Diego, 2 edition, 2002.

[6] D.L. Smith. *Thin-Film Deposition*. McGraw-Hill, New York, 1995.

[7] L. Hultman. Thermal stability of nitride thin films. *Vacuum*, 57:1–30, 2000.

[8] P.H. Mayrhofer, F. Rovere, M. Moser, C. Strondl, and R. Tietema. Thermally induced transitions of CrN thin films. *Scripta Mater.*, 57:249–252, 2007.

[9] E. Lugscheider, K. Bobzin, S. Bärwulf, and T. Hornig. Oxidation characteristics and surface energy of chromium based hardcoatings for use in semisold forming tools. *Surf. Coat. Technol.*, 133-134:540–547, 2000.

[10] L. Cunha, M. Andritschky, K. Pischow, Z. Wang, A. Zarychta, A.S. Miranda, and A.M. Cunha. Performance of chromium nitride based coatings under plastic processing conditions. *Surf. Coat. Technol.*, 133-134:61–67, 2000.

[11] R.F. Bunshah. *Handbook of Hard Coatings*. Noyes, New Jersey, 2001.

[12] J. Edwards. *Coating and Surface Treatment Systems for Metals.* Finishing Publications, Hertfordshire, 1997.

[13] J.L. Vossen and W. Kern. *Thin Film Processes II.* Academic Press, San Diego, 1991.

[14] I. Langmuir. Oscillations in Ionized Gases. *Proc. N.A.S.*, 14:627–637, 1928.

[15] A. Grill. *Cold Plasmas in Materials Fabrication.* IEEE Press, New York, 1994.

[16] B. Chapman. *Glow Discharge Processes.* John Wiley & Sons, 1980.

[17] P.A. Tipler and G. Mosca. *Physik.* Spektrum Akademischer Verlag, Heidelberg, 2006.

[18] G. Kienel and H. Oechsner. *Vakuumbeschichtung 2 - Verfahren und Anlagen.* VDI-Verlag, Düsseldorf, 1995.

[19] B. Rother and J. Vetter. *Plasmabeschichtungsverfahren und Hartstoffschichten.* Deutscher Verlag für Grundstoffindustrie, Leipzig, 1992.

[20] P.H. Mayrhofer. *Materials Science Aspects of Nanocrystalline PVD Hard Coatings.* PhD thesis, Montanuniversität Leoben, 2001.

[21] B. Window and N. Savvides. Charged particle flux from planar magnetron sputtering sources. *J. Vac. Sci. Technol. A*, 4(2):196–202, 1986.

[22] Gencoa – variable magnetrons at `http://www.gencoa.com/`.

[23] R.D. Arnell and P.J. Kelly. Recent advances in magnetron sputtering. *Surf. Coat. Technol.*, 112:170–176, 1999.

[24] P.J. Kelly and R.D. Arnell. Magnetron sputtering: a review of recent developments and applications. *Vacuum*, 56(3):159–172, 2000.

[25] J. Musil and J. Vlček. Magnetron sputtering of films with controlled texture and grain size. *Materials Chemistry and Physics*, 54(1-3):116–122, 1998.

[26] P. Losbichler and C. Mitterer. Non-reactively sputtered TiN and $TiB_2$ films: influence of activation energy on film growth. *Surf. Coat. Technol.*, 97:567–573, 1997.

[27] R.I. Masel. *Principles of Adsorption and Reaction on Solid Surfaces.* John Wiley & Sons, New York, 1996.

[28] D. Walton. *Nucleation.* Marcel Dekker, New York, 1969.

[29] L.B. Freund and S. Suresh. *Thin Film Materials.* Cambridge University Press, Cambridge, 2003.

[30] B.A. Movchan and A.V. Demchishin. Structure and properties of thick condensates of nickel, titanium, tungsten, aluminum oxides, and zirconium dioxide in vacuum. *Fiz. Metal. Metalloved*, 28:653–660, 1969.

[31] J.A. Thornton. Influence of substrate temperature and deposition rate on structure of thick sputtered Cu coatings. *J. Vac. Sci. Technol.*, 12(4):830–835, 1975.

[32] J.A. Thornton. Influence of apparatus geometry and deposition conditions on the structure and topography of thick sputtered coatings. *J. Vac. Sci. Technol.*, 11(4):666–670, 1974.

[33] E.S. Machlin. *Materials Science in Microelectronics: The Relationships between Thin Film Processing and Structure.* GIRO PRESS, New York, 1995.

[34] P.B. Barna and M. Adamik. Formation and characterisation of the structure of surface coatings. In Y. Pauleau and P.B. Barna, editors, *Protective Coatings and Thin Films*, pages 279–297. Kluwer Academic Publishers, Dordrecht, 1997.

[35] J.A. Thornton. High rate thick film growth. *Ann. Rev. Mater. Sci.*, 7:239–260, 1977.

[36] I. Petrov, P.B. Barna, L. Hultman, and J.E. Greene. Microstructural evolution during film growth. *J. Vac. Sci. Technol. A*, 21(5):117–128, 2003.

[37] J.-E. Sundgren and H.T.G. Hentzell. A review of the present state of art in hard coatings grown from the vapor phase. 4(5):2259–2279, 1986.

[38] C. Mitterer, P.H. Mayrhofer, E. Kelesoglu, R. Wiedemann, and H. Öttel. Internal growth parameters - a suitable basis for comparison of PVD coatings. *Z. Metallkd.*, 90:602–607, 1999.

[39] R. Messier, A.P. Giri, and R.A. Roy. Revised structure zone model for thin film physical structure. *J. Vac. Sci. Technol. A*, 2(2):500–503, 1984.

[40] C.R.M. Grovenor, H.T.G Hentzell, and D.A. Smith. The development of grain structure during growth of metallic films. *Acta Metallurgica*, 32(5):773–781, 1984.

[41] E. Lugscheider, O. Knotek, F. Löffler, C. Barimani, S. Guerreiro, and H. Zimmermann. Deposition of arc TiAlN coatings with pulsed bias. *Surf. Coat. Technol.*, 76-77:700–705, 1995.

[42] D. Hofmann, S. Kunkel, H. Schüssler, G. Teschner, and R. Gruen. Etching and sputter-ion plating using pulsed d.c. *Surf. Coat. Technol.*, 81:146–150, 1996.

[43] G. Reiners and M. Griepentrog. Hard coatings on magnesium alloys by sputter deposition using a pulsed d.c. bias voltage. *Surf. Coat. Technol.*, 76-77:809–814, 1995.

[44] J. Musil. Recent advances in magentron sputtering technology. *Surf. Coat. Technol.*, 100-101:280–286, 1998.

[45] J.N. Matossian, R. Wei, and J.D. Williams. Plasma-based ion implantation and electron-bombardment for large-scale surface modification of materials. *Surf. Coat. Technol.*, 96:58–67, 1997.

[46] R. Günzel, A.I. Rogozin, and V.T. Astrelin. Fast, uniform, and large-scale heat treatment by plasma-based electrons. *Vacuum*, 65:59–65, 2002.

[47] M. Olette. *Stickstoff in Metallen.* Akademie Verlag, Berlin, 1965.

[48] Landolt-Börnstein. *Phase Equilibria, Crystallographic and Thermodynamic Data of Binary Alloys Vol.5-D.* Springer, Berlin Heidelberg, 1994.

[49] T.B. Massalski. *Binary Alloy Phase Diagrams.* ASM International, Ohio, 2 edition, 1990.

[50] P. Hones, R. Sanjinés, and F. Lévy. Characterization of sputter-deposited chromium nitride thin films for hard coatings. *Surf. Coat. Technol.*, 94-95:398–402, 1997.

[51] T. Hurkmans, D.B. Lewis, J.S. Brooks, and W.-D. Münz. Chromium nitride coatings grown by unbalanced magnetron (UBM) and combined arc/unbalanced magnetron (ABS) deposition techniques. *Surf. Coat. Technol.*, 86-87:192–199, 1996.

[52] M. Odén, J. Almer, and G. Hakånsson. The effects of bias voltage and annealing on the microstructure and residual stress of arc-evaporated Cr-N coatings. *Surf. Coat. Technol.*, 120-121:272–276, 1999.

[53] J.J. Olaya, S.E. Rodil, S. Muhl, and L. Huerta. Influence of the energy parameter on the microstructure of chromium nitride coatings. *Surf. Coat. Technol.*, 200(20-21):5743–5750, 2006.

[54] A. Lippitz and T. Hübert. XPS investigations of chromium nitride thin films. *Surf. Coat. Technol.*, 200:250–253, 2005.

[55] G. Tischler. Herstellung und Charakterisierung reaktiv gesputterter Cr-N Hartstoffschichten. Master's thesis, Montanuniversität Leoben, 2001.

[56] P. Losbichler. *Ultraharte PVD-Schichten im System Ti-B-N.* PhD thesis, Montanuniversität Leoben, 1998.

[57] Veeco Metrology Group. *WYKO Surface Profilers Technical Reference Manual*, September 1999.

[58] Veeco Metrology Group. *WYKO NT1000 Setup Guide*, September 2000.

[59] K. Nitzsche. *Schichtmesstechnik.* Vogel, Würzburg, 1996.

[60] Deutsches Institut für Normung e. V. *DIN EN 1071 – Advanced technical ceramics – Methods of test for ceramic coatings.* Berlin.

[61] E. Lifshin. *X-ray Characterization of Materials.* WILEY-VCH, Weinheim, 1999.

[62] ICDD at `http://www.icdd.com/`.

[63] B.D. Cullity. *Elements of X-RAY DIFFRACTION.* Edision-Wesley, Reading, 2 edition, 1978.

[64] Siemens. *Operating Instructions D500/501 Diffractometer.*

[65] T.H. de Keijser, J.I. Langford, E.J. Mittemeijer, and A.B.P. Vogels. Use of the Voigt function in a single-line method for the analysis of X-ray diffraction line broadening. *J. Appl. Cryst.*, 15:308–314, 1982.

[66] P. Dasgupta. On use of pseudo-voigt profiles in diffraction line broadening analysis. *Fizika A*, 2:61–66, 2000.

[67] G.B. Harris. Quantitative measurement of preferred orientation in rolled uranium bars. *Mag. Phil.*, 43:113–123, 1952.

[68] J.A. Thornton and D.W. Hoffman. Stress-related effects in thin films. *Thin Solid Films*, 171(1):5–31, 1989.

[69] S. Tamulevičius. Stress and strain in the vacuum deposited thin films. *Vacuum*, 51:127–139, 1998.

[70] W.D. Nix. Mechanical properties of thin films. *Metallurgical and Materials Transactions A*, 20A(11):2217–2245, 1989.

[71] D. Winkler. Konzeption und Realisierung eines thermisch unterstützten Messverfahrens zur bestimmung von Eigenspannungen in dünnen Schichten. Master's thesis, Montanuniversität Leoben, 1997.

[72] T. Chudoba. Measurement of Hardness and Young's Modulus by Nanoindentation. In A. Cavaleiro and J.T.M. de Hosson, editors, *Nanostructured Coatings*. Springer, Berlin, 2006.

[73] A.C. Fischer-Cripps. Critical review of analysis and interpretation of nanoindentation test data. *Surf. Coat. Technol.*, 200:4153–4165, 2006.

[74] ISO Central Secretariat. *ISO 14577 – Metallic materials – Instrumented indentation test for hardness and materials parameters*. Geneva, 2002.

[75] A.C. Fischer-Cripps. *Nanoindentation*. Springer, Berlin Heidelberg, 2002.

[76] W.C. Oliver and G.M. Pharr. An improved technique for determining hardness and elastic modulus using load and displacement sensing indentation experiments. *J. Mater. Res.*, 7(6):1564–1583, 1992.

[77] A.C. Fischer-Cripps, P.Karvánková, and S.Veprek. On the measurement of hardness of super-hard coatings. *Surf. Coat. Technol.*, 200:5645–5654, 2006.

[78] UMIS product information at `http://www.ibisonline.com.au/`.

[79] J. Pelleg, L.Z. Zevin, and S. Lungo. Reactive-sputter-deposited TiN films on glass substrates. *Thin Solid Films*, 197(1-2), 1991.

[80] I. Iordanova, P.J. Kelly, R. Mirchev, and V. Antonov. Crystallography of magnetron sputtered TiN coatings on steel substrates. *Vacuum*, 81:830–842, 2007.

[81] J.E. Greene, J.-E. Sundgren, L. Hultman, I. Petrov, and D.B. Bergstrom. Development of preferred orientation in polycrystalline TiN layers grown by ultrahigh vacuum reactive magnetron sputtering. *Appl. Phys. Lett.*, 67(20):2928–2930, 1995.

[82] G. Knuyt, C. Quaeyhaegens, J. D'Haen, and L.M. Stals. A model for texture evolution in a growing film. *Surf. Coat. Technol.*, 76-77:311–315, 1995.

[83] A.J. Perry, V. Valvoda, and D. Rafaja. On the residual stress and picostructure of titanium nitride films. *Vacuum*, 45(1):11–14, 1994.

[84] T. Hurkmans, D.B. Lewis, H. Paritong, J.S. Brooks, and W.-D. Münz. Influence of ion bombardment on structure and properties of unbalanced magnetron grown $CrN_x$ coatings. *Surf. Coat. Technol.*, 114:52–59, 1999.

[85] L. Checkour, C. Nouveau, A. Chala, C. Labidi, N. Rouag, and M.A. Djouadi. Growth mechanism for chromium nitride films deposited by magnetron and triode sputtering methods. *Surf. Coat. Technol.*, 200:241–244, 2005.

[86] C. Gautier, H. Moussaoui, F. Elstner, and J. Machet. Comparative study of mechanical and structural properties of CrN films deposited by d.c. magnetron sputtering and vacuum arc evaporation. *Surf. Coat. Technol.*, 86-87:254–262, 1996.

[87] SRIM/TRIM simulation code at `http://www.srim.org/`.

[88] J.F. Ziegler. RBS/ERD simulation problems: Stopping powers, nuclear reactions and detector resolution. *Nucl. Instr. and Meth. in Phys. Res. B*, 136-138:141–146, 1998.

[89] J.F. Ziegler. SRIM-2003. *Nucl. Instr. and Meth. in Phys. Res. B*, 219-220:1027–1036, 2004.

[90] H. Holleck. Material selection for hard coatings. *J. Vac. Sci. Technol. A*, 4(6):2661–2669, 1986.

[91] J. Sillanpää, E. Vainonen-Ahlgren, P. Haussalo, and J. Keinonen. Stopping of 5-100 keV helium in molybdenum, chromium, copper and nickel. *Nucl. Instr. and Meth. in Phys. Res. B*, 142:1–8, 1998.

[92] G.C.A.M. Janssen. Stress and strain in polycrystalline thin films. *Thin Solid Films*, 515:6654–6664, 2007.

[93] P.J. Kelly, R. Hall, J. O'Brien, J.W. Bradley, G. Roche, and R.D. Arnell. Substrate effects during mid-frequency pulsed DC biasing. *Surf. Coat. Technol.*, 142-144:635–641, 2001.

[94] L. Cunha, M. Andritschky, K. Pischow, and Z. Wang. Microstructure of CrN coatings produced by PVD techniques. *Thin Solid Films*, 355-356:465–471, 1999.

[95] C. Mitterer, P.H. Mayrhofer, and J. Musil. Thermal stability of PVD hard coatings. *Vacuum*, 71:279–284, 2003.

[96] E. Martinez, R. Sanjinés, O. Banakh, and F. Lévy. Electrical, optical and mechanical properties of sputtered $CrN_y$ and $Cr_{1\text{-}x}Si_xN_{1.02}$ thin films. *Thin Solid Films*, 447-448:332–336, 2004.

[97] J.-W. Lee, S.-K. Tien, and Y.-C. Kuo. The effects of pulse frequency and substrate bias to the mechanical properties of CrN coatings deposited by pulsed DC magnetron sputtering. *Thin Solid Films*, 494:161–167, 2006.

[98] F.M. d'Heurle. Aluminum films deposited by rf sputtering. *Metall. Trans.*, 1(3):725–732, 1970.

[99] M.M.M. Bilek and D.R. McKenzie. A comprehensive model of stress generation and relief processes in thin films deposited with energetic ions. *Surf. Coat. Technol.*, 200:4345–4354, 2006.

[100] G. Abadias. Stress and prefered orientation in nitride-based PVD coatings. *Surf. Coat. Technol.*, 202:2223–2235, 2008.

[101] P. Hones, N. Martin, M. Regula, and F. Lévy. Structural and mechanical properties of chromium nitride, molybdenum nitride, and tungsten nitride thin films. *J. Phys. D: Appl. Phys.*, 36:1023–1029, 2003.

[102] P. Hones, R. Sanjinés, and F. Lévy. Sputter deposited chromium nitride based ternary compounds for hard coatings. *Thin Solid Films*, 332:240–246, 1998.